nature neuroscience

Article

https://doi.org/10.1038/s41593-026-02344-7

Connectomic evidence that ordered activity drives neuromuscular network formation

Received: 4 September 2024

Accepted: 14 May 2026

Published online: 30 June 2026

Check for updates

Yaron Meirovitch[1,4], **Kai Kang**[1,4], **Ryan W. Draft**[1,4], **Elisa C. Pavarino**[1], **Maria Fernanda Henao Echeverri**[1], **Fuming Yang**[1], **Stephen G. Turney**[1], **Daniel R. Berger**[1], **Adi Peleg**[1], **Marta Montero-Crespo**[1], **Yuelong Wu**[1], **Richard L. Schalek**[1], **Ju Lu**[2], **Jean Livet**[3], **Juan-Carlos Tapia**[1] & **Jeff W. Lichtman**[1]

We reconstructed complete connectomes between motor neurons and muscle fibers in small mouse muscles from birth through successive stages of postnatal development, when synaptic reorganization is most prominent. During development, marked reductions in axonal branching produced an approximately 6.5-fold decrease in the number of axons innervating each neuromuscular junction (NMJ), culminating in single innervation of all NMJs. Surprisingly, many neonatal muscle fibers also had more than one NMJ site. Most, but not all, of these supernumerary NMJs were eliminated. The few multiNMJ fibers that remained in adults had two widely separated junctions innervated by axons that exerted similar contractile forces and therefore had similar activity patterns. Unexpectedly, the muscle connectome further showed that both the loss of axons from individual NMJs and the elimination of entire NMJs related to the recruitment order of the innervating axonal cohort, and that this relationship reflected a rank-ordered pattern of axonal co-innervation. These observations argue that both local intrajunctional and long-distance interjunctional synaptic competition are activity-mediated and that the structure of mature neural circuits arises from the activity patterns of developing circuits.

The mammalian nervous system adapts to the animal's experience during postnatal life, as evidenced by the transition from clumsy to coordinated movement as well as the extensive modifications in sensory and autonomic systems[1,2]. The addition and removal of synapses in neural circuits, ubiquitous in developing animals, likely mediates such behavioral modifications. However, how sensory experiences and motor practices shape neural circuits remains poorly understood.

Postnatal synaptic reorganization has been extensively studied in the developing mammalian peripheral nervous system[3–6]. In early postnatal rodents, multiple alpha motor neurons send axonal branches to the same neuromuscular junction (NMJ). All but one of these axons eventually withdraw, leaving each adult NMJ with only one motor input[4]. This synapse elimination is driven by interneuronal competition for synaptic territory based on electrical activity[7–9], but how activity determines the fate of synapses is not understood. We took as our starting point two previous results: first, motor neurons are recruited in a fixed, size-ordered (small to large) manner irrespective of task difficulty[10] in both developing[11,12] and adult muscles[13,14]; second, at birth both the number of axons that converge on an NMJ and the number of NMJs an axon innervates are many times greater than that in later life[15]. To better understand the determinants of synaptic fate, we generated complete wiring diagrams of the connectivity between axons and their postsynaptic targets throughout the reorganization phase. This connectomic approach revealed

---

[1]Department of Molecular and Cellular Biology and Center for Brain Science, Harvard University, Cambridge, MA, USA. [2]Department of Biological Sciences, Lehigh University, Bethlehem, PA, USA. [3]Institut de la Vision, Sorbonne Université, INSERM, CNRS, Paris, France. [4]These authors contributed equally: Yaron Meirovitch, Kai Kang, Ryan W. Draft. e-mail: yaron.mr@gmail.com; jeff@mcb.harvard.edu

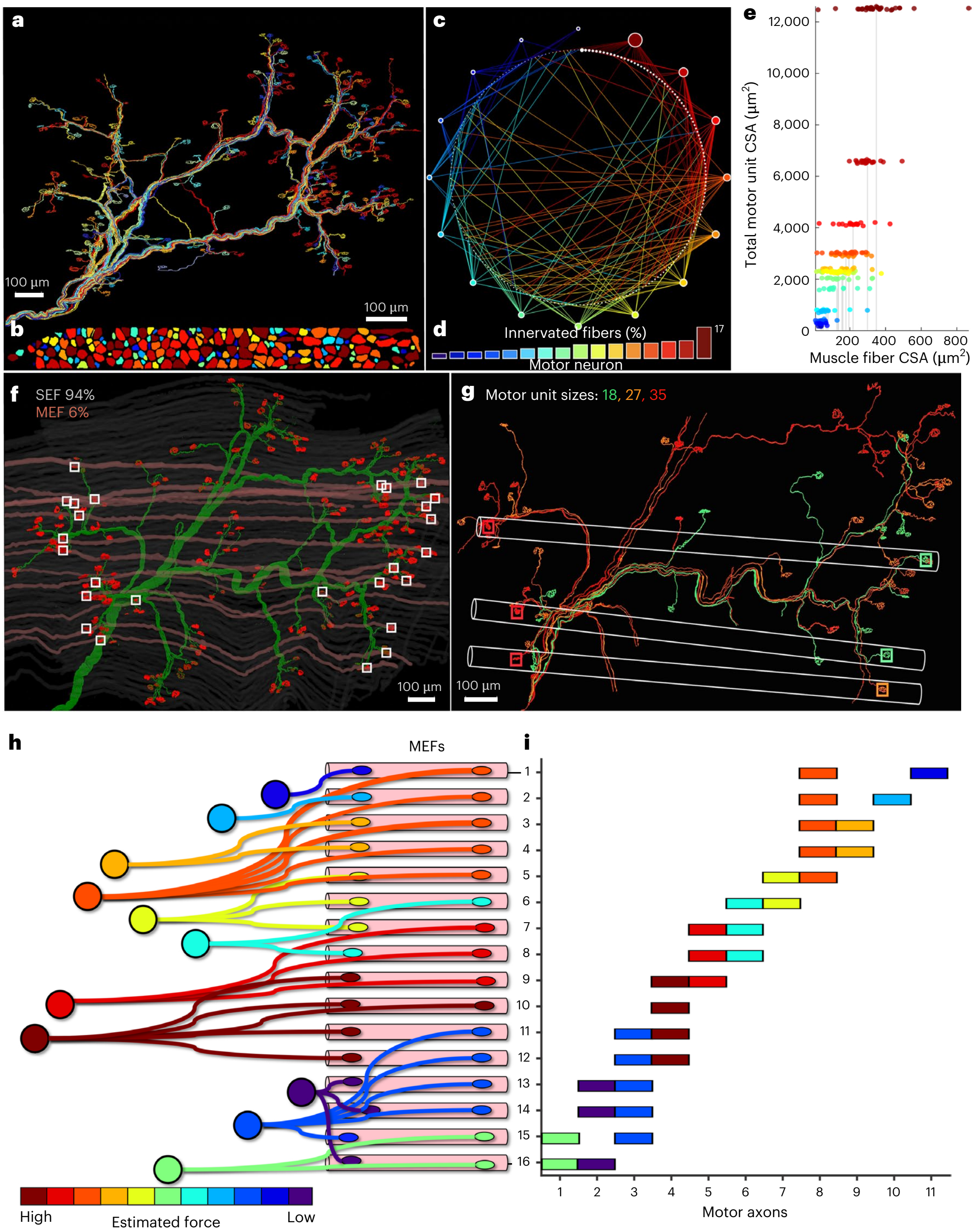

Fig. 1 | Neuromuscular connectome of an adult mouse (P60) interscutularis muscle. a, Confocal reconstruction of all 16 motor units. The colors of the axons represent the size of the motor units, with warm colors representing larger motor units and cool colors representing smaller ones. **b**, A cross section of the same thin muscle showing the CSAs of each muscle fiber, with colors representing the size of the input motor units. **c**, Graph representation of this adult muscle's connectome. The small nodes in the white inner circle represent each muscle fiber arranged by CSA, and the color-coded outer circle nodes represent the motor neurons. The connectivity of each motor axon is shown as straight-line edges. **d**, Motor units ranked by the percentage of innervated muscle fibers. The largest unit (dark red) innervates 17% of all muscle fibers. **e**, The total motor unit CSA, calculated as the sum of the CSAs of all fibers innervated by each motor neuron (*y* axis) as a proxy for the force generated by that motor unit. The range of muscle fiber diameters is shown for each motor unit (*x* axis). Colors represent, as in **a**–**d**, the sizes of the motor units. Vertical lines indicate the median muscle fiber CSA for each motor unit. Large motor units are associated with larger muscle fiber CSA, indicated by the super-linear relationship between the median muscle fiber size of a motor unit and the estimated force produced by the motor axon. **f**,**g**, Rendering of all the NMJs (red), nerve fibers (green), SEFs (gray) and MEFs (light brown) with their NMJs (white squares in **f**) in an adult interscutularis muscle. The NMJs on the MEFs are far apart (examples of three motor units in **g**). **h**, A diagrammatic representation of the connectome of the MEFs in the color-coded estimated forces of the motor units that innervate these fibers (as in **e**). **i**, Graph showing the tendency for the motor units that innervate the same MEF to have statistically similar force characteristics within a connected network. Note that the smallest motor units are at both ends of a contiguous interconnected network (discussed in later section).

two forms of synapse elimination occurring concurrently: the well-documented local intrajunctional competition, and a previously unknown long-distance interjunctional competition that removed entire NMJs. In both situations the fate of each axonal synapse was best explained by competition based on the relative synchrony and asynchrony of axons recruited in a fixed order.

Results

Ordering motor axons based on their putative contractile force

Using fluorescently labeled transgenic mice, we reconstructed the axonal arbors and muscle fiber targets of all the motor axons in two adult (postnatal day 60 (P60)) ear muscles (Fig. 1a,b): interscutularis A (Fig. 1a–e), with 235 muscle fibers innervated by 16 axons, and interscutularis B, with 217 muscle fibers innervated by 15 axons. We traced all axons to their innervated muscle fibers to determine the motor unit sizes (number of muscle fibers per axon; Fig. 1a–e). Motor axons were fasciculated into bundles but distributed their branches in the muscle in no particular pattern, often taking indirect routes to their muscle fiber targets, as previously described (Fig. 1a,b; see also ref. 16). A graph of this connectivity for one muscle is shown in Fig. 1c. In both muscles, motor units ranged in size, with the largest being six- to tenfold larger than the smallest (Fig. 1d). We measured the cross-sectional area (CSA) of each muscle fiber, a known correlate of its contractile strength[17–19]. The variation in an individual fiber's caliber along its length was small in comparison to the ~10-fold range of muscle fiber CSAs (Fig. 1b,e). The average CSA of muscle fibers within a motor unit correlated with motor unit size ($P < 0.05$; Extended Data Fig. 1c), yet the CSAs in a motor unit varied considerably, allowing even the largest and the smallest motor units to innervate some muscle fibers with similar CSAs (Fig. 1b,e). Because a motor unit's contractile force is a more relevant functional metric than its size, we estimated the total force of each motor unit by summing the CSAs of its constituent muscle fibers. This measurement amplified the functional differences amongst motor units to a ~50-fold range (Fig. 1e). Motor axons are thought to be recruited in a fixed order from the smallest to the largest contractile force (Henneman's size principle[10,13]); this order was largely the same whether ranked by the total CSA or the motor unit size (Supplementary Fig. 1). While this connectomic result cannot reveal the precise timing of motor control, it argues that motor unit size may underestimate the range in motor unit contractile forces and thus may predict motor unit recruitment time less accurately than total CSA.

Muscle fibers sometimes have more than one NMJ

Many previous studies of mammalian muscles have assumed only one NMJ per muscle fiber. However, our connectomic reconstruction revealed that 13 muscle fibers in muscle A (5.5%) and 16 in muscle B (7.4%) possessed two NMJs (hereafter termed multiple-endplate muscle fibers, MEFs), and the rest had one NMJ (hereafter termed single-endplate muscle fibers, SEFs). Moreover, the two NMJs on each MEF were significantly farther apart than expected by chance (1.5-fold in A and 1.7-fold in B; median distance versus median distance of random pairs in A: $P < 1.5 \times 10^{-5}$, B: $P < 6.8 \times 10^{-5}$; Wilcoxon rank-sum; Fig. 1f,g). Interestingly, across the two adult muscles, the estimated contractile forces of the motor unit pairs innervating the same MEFs were more similar to each other than expected by chance ($P < 0.0003$; Fig. 1h,i and Methods), as was also observed if we just compared motor unit sizes ($P < 0.001$; Supplementary Fig. 1). Moreover, the same motor unit pairs repeatedly co-innervated the same MEFs (Fig. 1h,i and Supplementary Fig. 2). Because of Henneman's size principle, the similarity in estimated motor unit forces at MEFs on the same muscle fiber suggests that these axons are close to each other in the recruitment order and therefore have similar activity patterns. This view implies that axonal terminals with similar activities can co-innervate the same muscle fiber, but only when physically far apart from each other.

NMJ elimination during development and its distance dependence

To explore how rare MEFs arose during development, we surveyed 25 muscles and their 7,462 NMJs, looking for MEFs at successive developmental ages (Supplementary Table 1). MEFs were on average 4.8-fold more abundant at birth than in adulthood ($n = 5$ muscles at each age), with the number dropping precipitously during the first 2 postnatal weeks (Fig. 2a,b). Using serial-section electron microscopy (ssEM, described later), we found that 34.4% of the newborn muscle fibers were MEFs, possessing two (27.6%) or sometimes three (6.7%) NMJs. Consistent with this result, using confocal microscopy in five additional newborn muscles, we found 31.2–39.2% of the muscle fibers were MEFs. The percentage remained high at P3 (42.4%) but then declined rapidly to ~6% in adults, where no muscle fiber with three NMJs remained. The slight decrease in total muscle fiber number (7.5%) could not account for the ~84% reduction in the number of MEFs, ruling out muscle fiber loss as the primary explanation. These results indicate that wholesale NMJ loss, in which all the axons that innervate an NMJ are eliminated, is a second important method of postnatal synapse elimination in the interscutularis muscle. This process occurs during the same 2-week interval as intrajunctional synapse elimination and substantially reduces the number of axons contacting individual muscle fibers.

At early postnatal ages, not only were there far more MEFs, but their NMJs were on average much closer together, even when the distance was normalized to the length of the muscle at each age (Fig. 2a). Among the MEFs in the P0 ssEM dataset, 29 pairs of NMJs (~37.6%) were separated by less than 50% of the maximal interjunctional distance (0.975 mm), whereas in adults, no pairs were ever separated by less than 50% of their maximal distance (~1.88 mm; $P < 0.0001$). Bootstrap analysis using size-matched random subsets of the P0 population confirmed that this shift was not a sampling artifact due to fewer MEFs in adulthood. Indeed, normalized adult MEF distances were significantly greater ($P < 0.01$, Wilcoxon signed-rank test; Extended Data Fig. 2), indicating preferential retention of MEFs with the largest interjunctional distances. NMJ loss, therefore, strongly depends on the interjunctional distance. However, while over 20% of newborn muscle fibers possessed NMJs separated by at least 0.5 mm, this distance did not prevent endplate elimination, as only 6% of muscle fibers remained MEFs in adults. This indicates that many muscle fibers with widely separated NMJs at early ages (>0.5 mm) still lost one by adulthood. Thus, interjunctional distance is a necessary but not sufficient factor, and other factors must be at play. Moreover, we observed no adult muscle fibers lacking all of their NMJs, suggesting that the loss is guided by some form of interjunctional competition.

Examination of the latest age when NMJs were still occasionally nearby on the same muscle fiber provided insight into the NMJ elimination mechanism. In P10–P12 muscles, we found six MEFs with pairs of nearby NMJs (incidentally, each was singly innervated). In each of these muscle fibers, the same axon innervated both NMJs (Fig. 2c). As we did not observe any MEFs with nearby NMJs in later life, we infer that eventually one of the two NMJs would be eliminated, despite sharing the same input (and hence the same position in the recruitment order).

Interestingly, intrajunctional synapse elimination was accelerated on MEFs compared with SEFs. At P10, 73% of the NMJs on MEFs were singly innervated, versus only 44% on SEFs ($P < 10^{-8}$; Fig. 2d). One interpretation is that activity at one NMJ influences the fate of synapses at the other NMJ on the same muscle fiber. Such interjunctional synapse elimination could be mediated by propagating action potentials (APs) affecting the fate of the axons at a distant junction.

An activity-mediated mechanism for long-distance intersynaptic competition

While activity is posited to be central to synaptic competition within individual NMJs[3,7,9,20–26], known mechanisms cannot explain the wholesale NMJ elimination observed here, which depends on both distance

https://doi.org/10.1038/s41593-026-02344-7

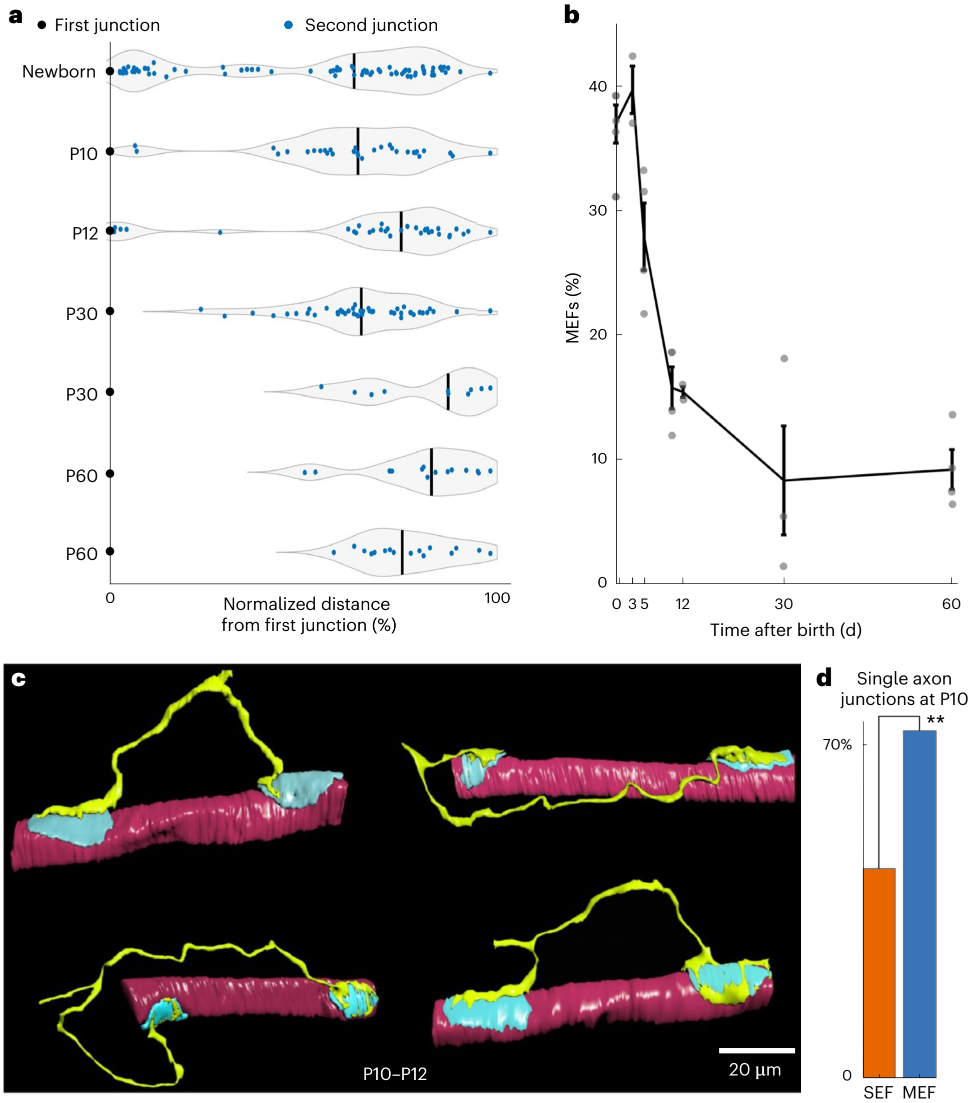

Fig. 2 | Loss of NMJs during early postnatal life. a, Diagram showing the location of the second NMJ on all MEFs (blue dots) along the muscle's length at multiple developmental ages. The lengths are normalized to the maximum distance between NMJs at each age, with the first NMJ marked by a black dot and the median by a black bar. Notice the disappearance of all nearby NMJs. **b**, The profound loss of MEFs owing to the loss of NMJs in early postnatal life. Error bars represent mean ± s.d. at each age. A total of 25 ear muscles were analyzed across the developmental series. **c**, Four representative examples showing that the last remaining pairs of nearby NMJs on MEFs at P10–P12 were in each case innervated by the same axon at both junctions. Six such junction pairs were identified across these ages. **d**, Histogram showing that a greater fraction of NMJs on MEFs than on SEFs were singly innervated at P10 (**$P < 10^{-8}$, two-sided Fisher's exact test), indicating accelerated intrajunctional synapse elimination on MEFs.

and axon identity. The fact that NMJs on neighboring muscle fibers can be adjacent (Fig. 1b), while two on the same muscle fiber must be far apart to coexist, implies that interjunctional synaptic competition is mediated by signals passing through the co-innervated muscle fiber. One such signal is propagating APs initiated at NMJs that are known to be capable of eliminating nonsynaptic (extrajunctional) neurotransmitter receptors at distant sites[27]. But could an AP initiated at one NMJ be the propagating signal that destabilizes a distant NMJ? If so, why does this destabilization sometimes fail, allowing two NMJs to persist on the same muscle fiber? And why does it allow the elimination of one of a pair of nearby NMJs even when the same axon innervates both? We considered the possibility that such interjunctional communication would be prevented if both junctions elicit APs relatively synchronously, each triggering a refractory period that causes the APs to collide and annihilate. Previous studies have shown that APs elicited at two ends of the muscle fiber do collide, preventing them from passing each other[28–31]. We thus propose a model where wholesale NMJ elimination occurs only when asynchronous postsynaptic firing allows the APs from one junction to invade the other (Fig. 3a).

As a concrete example, when a pair of nearby NMJs existed on a muscle fiber, one was always eliminated in the first few postnatal weeks (Fig. 2a,b), even if the two junctions were innervated by the same axon (Fig. 2c). Based on the collision hypothesis, this loss requires that an AP from one junction reach the other before the second can elicit an AP. To test whether this was possible, we analyzed four P10–P12 MEFs, each with two nearby NMJs (41–72 μm apart) that were both innervated by the same motor neuron (Fig. 2c). The annihilation of both APs by collision, and hence the maintenance of both NMJs, would only occur if the onset of the two muscle fiber APs consistently differed by less than the AP propagation time between the two NMJs (27–48 μs, for a physiologically reasonable muscle fiber conduction velocity of 1.5 m s^{-1} (refs. 32,33); Supplementary Table 2). We analyzed the parameters that set the time gap in these four cases where the two junctions were innervated by the same axon. First, differences in axonal branch

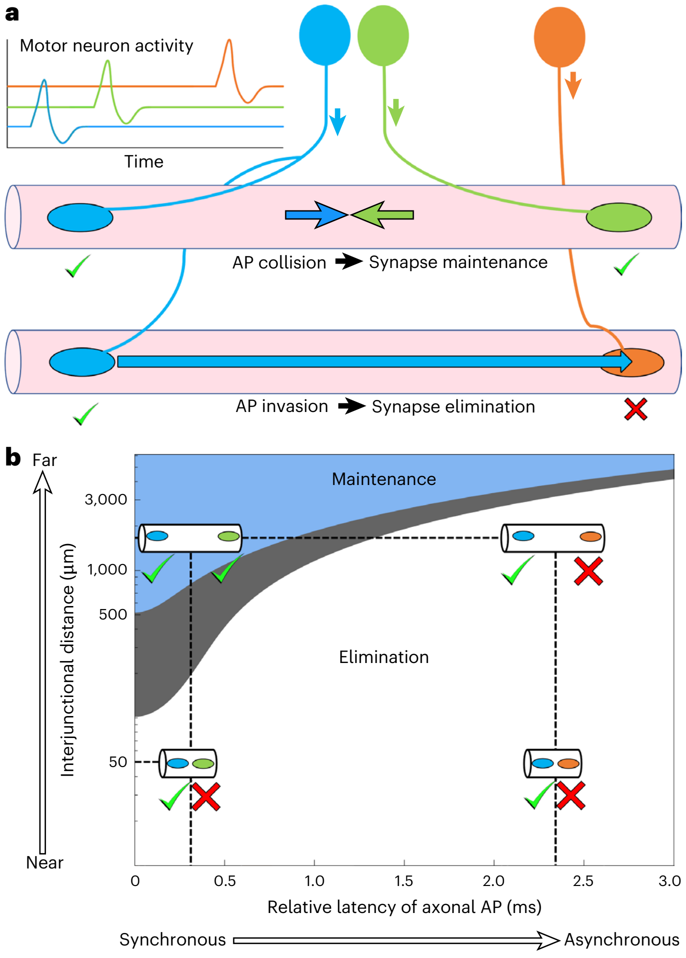

Fig. 3 | Mechanism for the regulation of NMJ maintenance or elimination by neural activity patterns and intersynaptic distance during development. **a**, Diagram showing the recruitment order of three motor axons (blue, then shortly later green, then with a larger pause, orange) that are co-innervating the same MEFs. The small pause between the blue and the green neuron's activation means that the APs that initiate in a muscle fiber (top fiber) will collide and thus neither of the two inputs will be able to invade the NMJ innervated by the other axon, leading to stable maintenance of both junctions. However, when the blue and orange axons innervate different NMJs on the same MEF, the larger delay in their initiation of muscle fiber APs means that the muscle fiber AP initiated by the blue axon will invade the NMJ innervated by the orange axon and destabilize it. **b**, Model that predicts the distances and latencies that give rise to NMJ elimination (when collision rate is <20%; white area), maintenance (when collision rate is >80%; blue area) or an indeterminate outcome (collision rate 50 ± 30% of the time; gray area) on MEFs based on AP propagation times, stochastic synaptic delays and the probabilities of AP collisions (see Supplementary Fig. 3 for all collision rates).

length created a presynaptic arrival time gap that, in three of four cases, already exceeded the propagation time[34–36]. In addition, even if presynaptic APs arrive simultaneously at the nerve terminals, collision would still be unlikely because postsynaptic AP initiation is delayed by a significant but variable synaptic delay (~0.5 ms ± an s.d. of ~0.13 ms)[37]. We estimated the resulting difference in postsynaptic AP onset between two such NMJs to be on average ~0.15 ms (s.d. × $(4/\pi)^{1/2}$). This time gap, similar to the branching-based time gap, is greater than the short conduction time between nearby junctions. The predicted probability of AP collision is low (≤14% collision rate; Supplementary Table 2 and Methods). Even with true presynaptic synchrony, we expect AP invasion and NMJ elimination of one of a pair of nearby NMJs (Fig. 3b, Supplementary Fig. 3 and Methods, 'Modeling AP collision as the mechanism to maintain multiple NMJs on the same muscle fiber').

On the other hand, when two NMJs are innervated by the same axon but are far apart, the probability of collision increases because the interjunctional conduction time is now greater than the expected postsynaptic AP initiation time difference between the two junctions (that is, ~0.15 ms). This means that the two NMJs can coexist. For example, the collision rate is >95% for NMJs that share the same axon but are >790 µm apart. Among the few adult MEFs, 14% ($n = 4$) had the same axon innervating both NMJs. However, this model requires only sufficient synchrony to ensure collision; it does not require the same axon to innervate two far apart NMJs. In particular, if the two NMJs are 0.94 mm apart (the minimum distance observed at adult MEFs), achieving a >50% or >95% collision rate requires their presynaptic APs to arrive at the junctions within 0.63 ms or 0.18 ms of each other, respectively, consistent with measured recruitment delays between mammalian motor units[38].

We conclude that the degree of similarity in axonal activity patterns at distributed synaptic sites on the same muscle fiber determines the long-term fate of these synapses. This simple model explains the sensitivity of the final outcome to both interjunctional distance and the recruitment order. We next explored whether recruitment order also was a determinant of synapse elimination when axons occupied the same NMJ site.

Network-wide rank ordering of the neuromuscular connectome in development

We used Brainbow transgenic mice[39,40] to study all the motor units supplying polyneuronal innervation to NMJs in mouse muscles between P6 and P9. About half (47%) of the junctions are multiply innervated at this stage, which is intermediate between the singly innervated adult NMJs (typically by P14), and the polyneuronal innervation of all newborn NMJs (described later). In contrast to the interscutularis, ventral neck (omohyoid) and paw (lumbrical) muscles have excellent Brainbow expression and fewer motor units, permitting the identification of all motor units by their distinct fluorescent hues (Extended Data Figs. 3 and 4 and Methods). We reconstructed seven connectomes: four omohyoids (Om1–4) and three lumbricals (Lum1–3); motor unit sizes and convergence rates are listed in Supplementary Table 3.

Motor units in each of these muscles varied in size. For example, in Om4 (P6), the largest motor unit (pink) possessed 145 muscle fibers, and the smallest (magenta) had 88 (Fig. 4a,b and Extended Data Fig. 5). The propensity for single innervation also varied: one motor unit (red) singly innervated ~30% (38 of 127) of its targets, whereas another (green) singly innervated only 1.6% (2 of 125). This variability between motor units suggests a complex picture of neuromuscular synapse elimination.

We first explored the identity of the axons sharing NMJs at this mid-developmental stage. Surprisingly, in all seven connectomes the subset of axons co-innervating each NMJ adhered to a consistent nonrandom ordering rule. For example, in Om4 (Figs. 4b and 5a,b), the red motor neuron shared many NMJs with the blue motor neuron (66 junctions), but progressively fewer NMJs with the pink (26), light purple (16), green (4) and magenta (1) motor neurons (Fig. 5a,b; other muscles in Extended Data Fig. 6). Remarkably, the magenta motor neuron exhibited the opposite order of preferences, sharing 60, 19, 6, 0 and 1 NMJs with the green, light purple, pink, blue and red motor neurons, respectively (Figs. 4b and 5a). Moreover, this rank order (red, blue, pink, light purple, green and magenta) explained the co-innervation preferences for all the other axons (Fig. 5b). In all cases, motor neurons shared far more muscle fibers with their immediate neighbors in the order than with more distant axons (Fig. 4b). The rank order was not explained by the topography of innervation in the muscle (Extended Data Figs. 4 and 5). In all seven muscles, a single ordered arrangement dictated whether axons co-innervated muscle fibers. Such preferences were unlikely to emerge by chance ($P < 0.005$ in each muscle; Supplementary Fig. 4 and Methods). Given that neurons innervate more NMJs at birth (see below),

https://doi.org/10.1038/s41593-026-02344-7

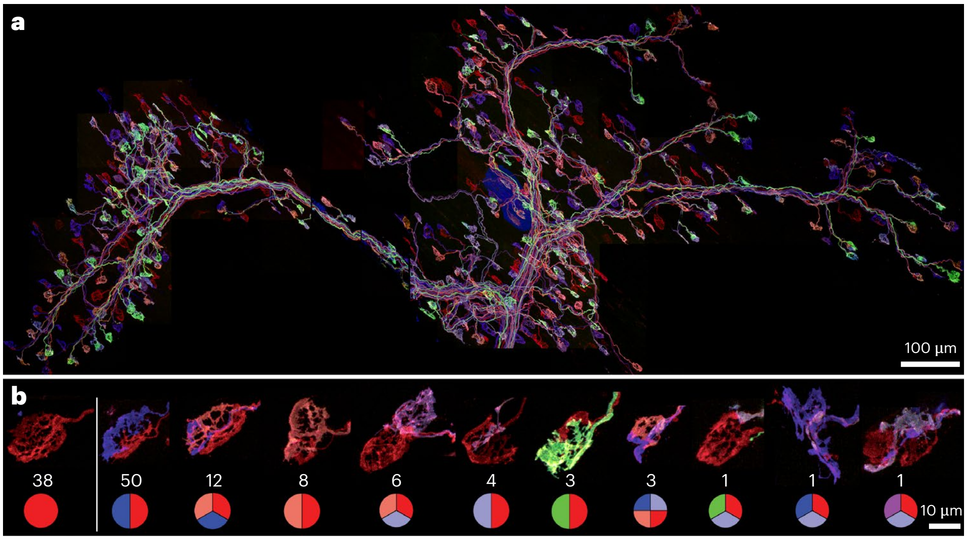

Fig. 4 | Brainbow labeling of motor axons and co-innervation patterns in a P6 omohyoid muscle. a, Confocal reconstruction of the connectome. The motor axons showed six distinct colors. At this age individual NMJs are either singly or multiply innervated. **b**, The distribution of axonal inputs to the subset of NMJs that are innervated by the red-labeled axon. In addition to 38 singly innervated junctions (far left), the red axon also co-innervated many junctions with other colored axons. Examples of the types are displayed from the most to least common (left to right).

these ordered arrangements at P6–P9—whatever their cause—signify graded neuronal preferences regarding where they continue to maintain synapses and where they do not.

We considered two alternative reasons for the observed rank orders: chemospecific matching of motor neurons and muscle fiber types, and/or activity-dependent synapse elimination related to the recruitment order. To determine the role of chemospecificity in generating the rank order, we examined motor axons that did not share NMJs (that is, at opposite ends of the rank order). We stained three P8–P9 lumbrical muscles with fluorescently tagged anti-myosin I immunoglobulin to identify the slow muscle fibers. Brainbow labeling revealed several small motor units innervating myosin I-positive muscle fibers in each lumbrical. In one of them (Lum1, P9), we found two motor units that both innervated slow muscle fibers, yet were positioned at opposite ends of the connectivity rank (Supplementary Fig. 4) and shared significantly fewer NMJs than expected by chance ($P < 0.0001$; matched motor unit size connectomes). The fact that two motor units targeting the same fiber type avoided co-innervation rules out simple fiber-type chemospecificity as the organizing principle.

Alternatively, the relative synchrony of axons at an NMJ may determine the outcome of synapse elimination, an idea consistent with previous studies showing a role for activity on synapse maintenance and elimination[7,9,41]. Specifically, axons recruited next to each other will be more synchronized and thus coexist longer than asynchronously active axons at the same NMJ. The absence of NMJs co-innervated by the two slow motor units in Lum1 (P9) suggests, surprisingly, that these units are highly asynchronous, despite the fact that slow motor units are recruited early[42]. In several of the other connectomes, small motor units were at the opposite ends of the rank order. For example, in the rank order mentioned above for Om4 (P6; Figs. 4b and 5a,b), the largest motor unit (pink) was at the center of the rank, while two small motor units (red and magenta) were at the extremes and shared significantly fewer NMJs than expected by chance ($P < 0.00001$; Methods). This finding was replicated in another muscle, Lum3 ($P < 0.01$; Extended Data Fig. 6 and Supplementary Figs. 4 and 5). This lack of co-innervation among the smallest motor units, if it is explained by asynchrony in activity, challenges the standard view of the size principle where the motor units are recruited in order beginning with the smallest motor units. So we were in a quandary as neither chemospecificity nor activity seemed to explain the result. However, searching the literature on motor unit recruitment, we found several interesting papers showing that small, fatigue-resistant motor units engage in asynchronous, cyclical activity known as 'motor unit rotation'[43,44], which would limit their synchronous firing and thus inhibit the maintenance of their axons at the same NMJs, as was found in our results ('Discussion').

In summary, the innervation pattern at P6–P9 suggests that NMJs progressively eliminate axons whose activity pattern differs from the prevailing activity pattern on that fiber. Based on the fact that in maturity the last-recruited motor unit is the largest, we hypothesize that within an NMJ, the last-recruited axon is favored to persist. Notably, this outcome is opposite to the rule we inferred for interjunctional synapse elimination where the first-recruited axon appears to have the advantage ('Discussion').

Massive synaptic convergence and divergence at birth

Given the well-known refinement of neuromuscular connections after birth, we used ssEM to reconstruct a P0 connectome (20 axons, 240 muscle fibers) to determine how this rank ordering was established (Fig. 6a, Extended Data Fig. 1a and Supplementary Fig. 6). In this connectome, all muscle fibers were innervated by more than one axon, in contrast to 6.4–13.6% in adults (P60; $n = 4$). In addition, all but one of the NMJs ($n = 309$; 99.7%) were multiply innervated, with between 1 and 13 axons converging onto each NMJ (mean 6.53 ± 2.217; Supplementary Fig. 7), whereas adult connectomes contained no multiply innervated NMJs. Moreover, 34.4% of the P0 muscle fibers had more than one NMJ (Fig. 2a and Extended Data Fig. 1b). This combination of MEFs and high convergence at individual junctions allowed many axons to converge on individual muscle fibers. In fact, some muscle fibers received innervation from 75% ($n = 15$) of all the motor neurons in the muscle. Thus, after birth, the number of axons per NMJ and the number of NMJs per muscle fiber both decreased substantially. These two forms of synapse elimination reduced motor unit sizes 6.57-fold, from 92 ± 32 fibers (range: 13–120, $n = 20$ motor units) at birth to 14 ± 8 fibers (range: 3–39; $n = 34$ motor units) at P60. Unlike adult muscles, which each possessed only one large motor unit (~40 muscle fibers; Fig. 1d), the newborn muscle contained five similarly large motor units (117–120 muscle fibers; Fig. 6b). Of the potential 4,800 connections between the 20 motor axons and 240 muscle fibers in the P0 connectome, we observed 1,833 connections, or ~38.2% of

https://doi.org/10.1038/s41593-026-02344-7

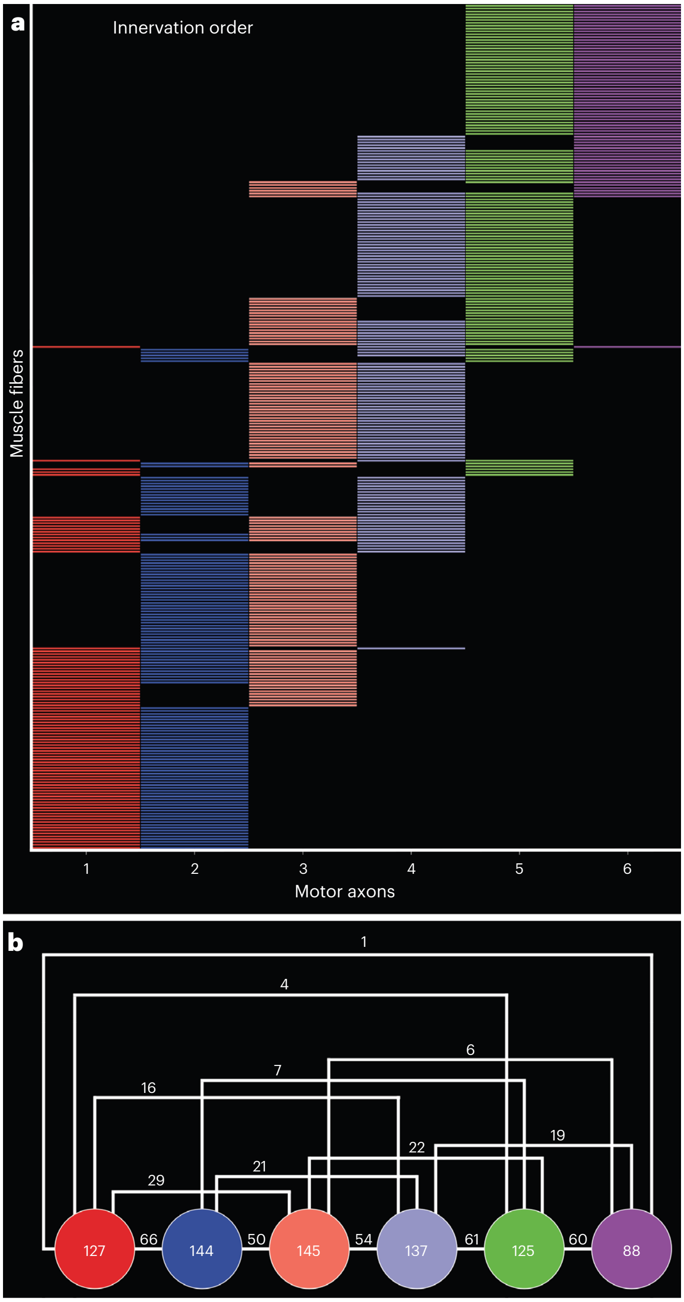

Fig. 5 | Rank-ordered organization of shared NMJ innervation in a P6 omohyoid muscle. a, We ranked the motor axons (Fig. 4a) in terms of their tendency to innervate the same muscle fibers. Shown in horizontal lines are the innervations to all the individual muscle fibers that are multiply innervated. The six motor neurons in the rank order shown co-innervate more muscle fibers with their nearby neighbors than more distant ones. **b**, Quantification of the connectivity of the rank-ordered motor axons in **a**, showing along the lines the number of co-innervated muscle fibers for every axonal pair (other muscles are shown in Extended Data Fig. 6). The numbers in the circles indicate the full motor unit size for each axon.

the theoretical all-to-all maximum (Fig. 6c). This extensive fan-in and fan-out pattern contrasts with the sparse pattern in later life, where only 6.8–7% of the potential connections between motor neurons and muscle fibers were realized (compare Fig. 6c with Fig. 1c and see Extended Data Fig. 7). Despite the much larger motor units at birth, the range in sizes of motor units in both newborns and adults was roughly tenfold (compare Fig. 1d and Fig. 6b and see Extended Data Fig. 1b and Supplementary Fig. 8).

Given that at P0 motor units already varied in size, we sought to learn whether there was any structure in the newborn connectome. We found evidence for the same rank-ordered connectivity seen at later ages, albeit a considerably weaker version (Fig. 6d). Many P0 axonal pairs co-innervated significantly more or fewer muscle fibers than expected by chance ($P < 0.001$; Methods). These preferences formed a continuous connectional network as present at later ages (Extended Data Fig. 8 and Supplementary Fig. 9). This pattern ruled out the idea that the P0 connectome is simply a random, largely overlapping network. Instead, buried in the dense wiring between neonatal neurons and muscle fibers was a tendency for neurons to share muscle fibers based on a rank order ($P < 0.05$) (Supplementary Fig. 10a,d and Methods), presaging the ordered innervation patterns seen in older animals.

Other features of the newborn connectome also anticipate the adult pattern. In both our adult data and the previously described adult interscutularis connectome[16], motor neurons with larger motor units had larger CSAs at their entrance point into the muscle (Extended Data Fig. 1c; $r = 0.89$, $P < 10^{-7}$). In adults, the largest motor units innervated, on average, the largest-diameter muscle fibers, whereas the smallest motor units innervated the smallest fibers (Fig. 1e and Extended Data Fig. 1). In the newborn, we found a significant tendency in the same direction (Extended Data Fig. 1b,c): the larger motor units innervated larger-diameter muscle fibers (group correlation, Extended Data Fig. 1c, $r = 0.629$, $P = 0.0029$; 10 of 20 motor units were selective for large muscle fibers, Extended Data Figs. 8d and 9b, $P < 0.01$; motor unit selectivity to muscle fiber size compared with random connectomes, $P < 0.001$). At least one small motor unit innervated muscle fibers that were, on average, significantly smaller ($P < 0.05$). About half the motor neurons at birth, however, did not show any specificity for muscle fibers of a particular diameter. These results suggest that the size principle has already begun to emerge even though neonatal muscle fibers are innervated by many more axons than in later life. Nonetheless, the adult distribution of motor unit sizes could not be generated by random synapse elimination from the P0 connectome, as indicated by our simulation (repeated 300 times; Extended Data Fig. 10 and Supplementary Fig. 11). Rather, these simulation results are consistent with the idea that postnatal activity patterns play a central role in establishing the adult motor unit properties. If such activity begins prenatally, it may also help explain the nascent patterning already present at birth. Indeed, prenatal motor activity is commonplace in all mammals, a point expanded upon in the 'Discussion'. This suggests that the process of fine-tuning how the CNS connects to muscles is closely linked to brain activity and movement both before and after birth.

Discussion

In this work, we used connectomic methods to analyze the complete set of axons innervating muscle fibers at several postnatal developmental stages of mice. We observed phenomena related to (1) a larger extent of postnatal circuit remodeling than expected; (2) the competitive elimination of entire NMJs; (3) rank ordering of connectivity; (4) a long-distance requirement for maintaining multiple NMJs on individual muscle fibers; and (5) an early, perhaps prenatal, onset of the synaptic reorganization program. We believe these findings can all be explained by a unifying principle of patterned-activity-driven synapse elimination.

NMJ loss and maintenance are driven by the timing of intersynaptic activity

We found that in addition to the transition to singly innervated NMJs, the number of muscle fibers with more than one NMJ decreased by ~80%. All told, of the axonal branches innervating the entire muscle at birth, axon withdrawal occurred approximately 1,800 times, leaving about 10% of the branches in adults. About a third of the pruned

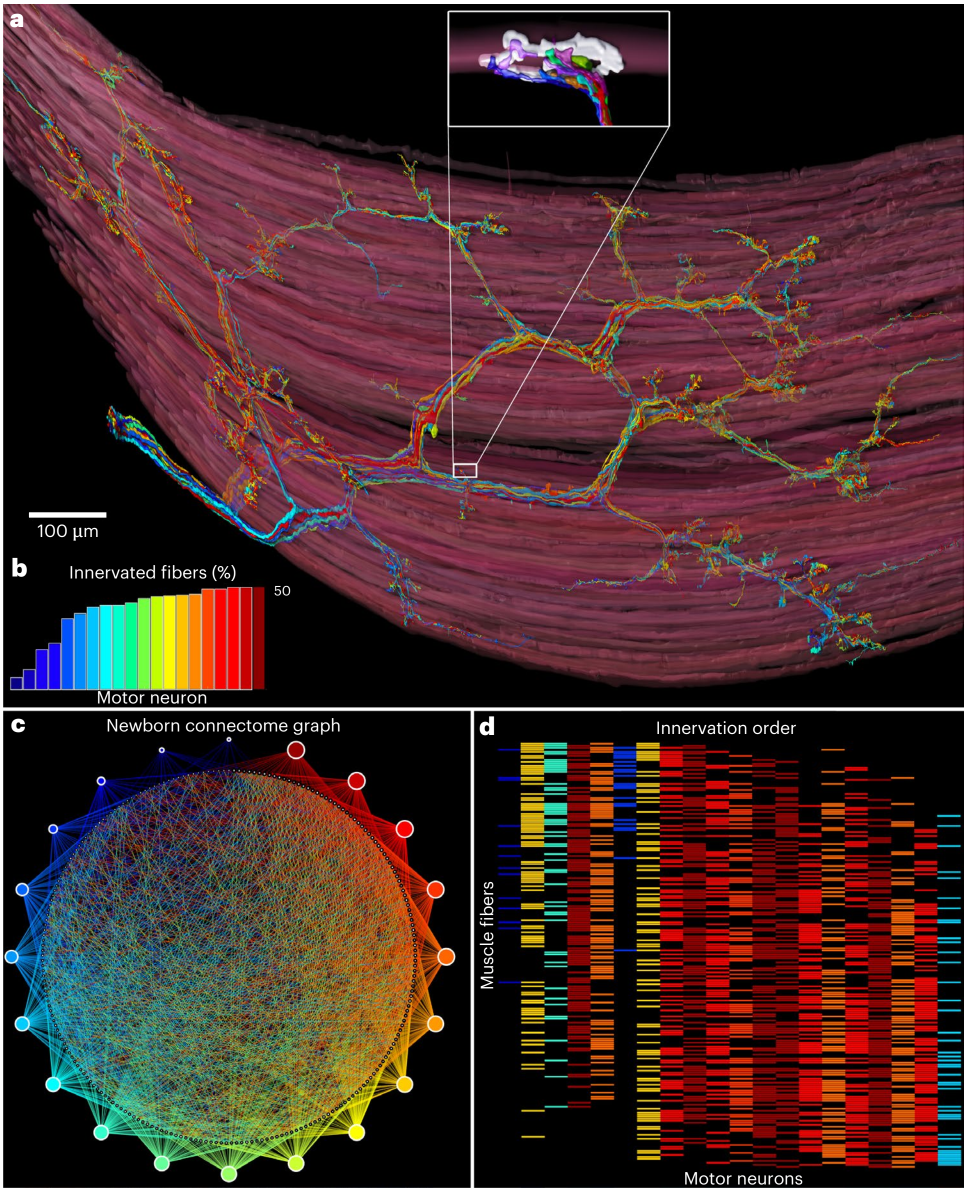

Fig. 6 | Neuromuscular connectome of the newborn mouse (P0) interscutularis muscle. a, An ssEM reconstruction of all 20 motor units. The colors of the axons represent the size of the motor units, with warm colors representing larger motor units and cool colors representing smaller ones as in Fig. 1. **b**, Motor units ranked by the percentage of innervated muscle fibers. The largest unit innervates 50% of all muscle fibers, with a greater number of large units than small ones. This distribution is opposite to that in adults, where only 1–2 units are distinctly large, and most units are small (Fig. 1d). **c**, Graph representation of this muscle's connectome. The small nodes in the inner circle represent each muscle fiber (arranged by CSA), and the nodes in the outer circle represent the motor neurons. The connectivity of each motor axon is shown as straight-line edges. Compare this with the dramatically different graph in adults (Fig. 1c and Extended Data Fig. 7). We observed 38.19% (1,833 connections) of the theoretical all-to-all connectivity. **d**, Similar to Fig. 5a, we ranked the motor axons such that pairs of axons co-innervating muscle fibers beyond what is expected by chance are next to each other in the rank order. We then sorted the set of muscle fibers such that muscle fibers with similar axonal inputs are placed next to each other. Already at birth, the co-innervation map prefigures the ordered innervation map seen in later developmental stages (Fig. 4b) and in adults (Fig. 1i), although the effect is much weaker.

branches could be accounted for by loss of NMJs. The loss of multiple NMJs on a muscle fiber reduces unnecessary redundancy. The small number of adult muscle fibers that maintain two NMJs might just be an unavoidable consequence of the mechanism. Usually in early postnatal life, asynchronous neural activity allows an AP from one NMJ to invade a synaptic site innervated by another axon causing the latter's destruction, leading to axon withdrawal and AChR cluster disappearance. Moreover, this same mechanism likely also occurs prenatally when all muscle fibers transiently have multiple acetylcholine receptor-rich sites[45,46]. The long-term maintenance of MEFs occurs only when the timing of the postsynaptic activity elicited by different junctions is similar, allowing their APs to collide. This mechanism explains why two NMJs can persist only when they are very far apart because long distance assures AP collision (when the interval between AP initiation at the two junctions is less than the AP propagation time between the NMJs). Further evidence that activity from one NMJ drives the elimination of another NMJ is the accelerated rate of axon withdrawal at junctions on MEFs compared with SEFs (Fig. 2d). Finally, we were struck by similar rank-ordering connectivity motifs, both between the remaining MEFs in adults (Fig. 1h) and at multiply innervated NMJs in development (Figs. 5a and 6d), suggesting that motor axons with similar activity patterns coexist on the

https://doi.org/10.1038/s41593-026-02344-7

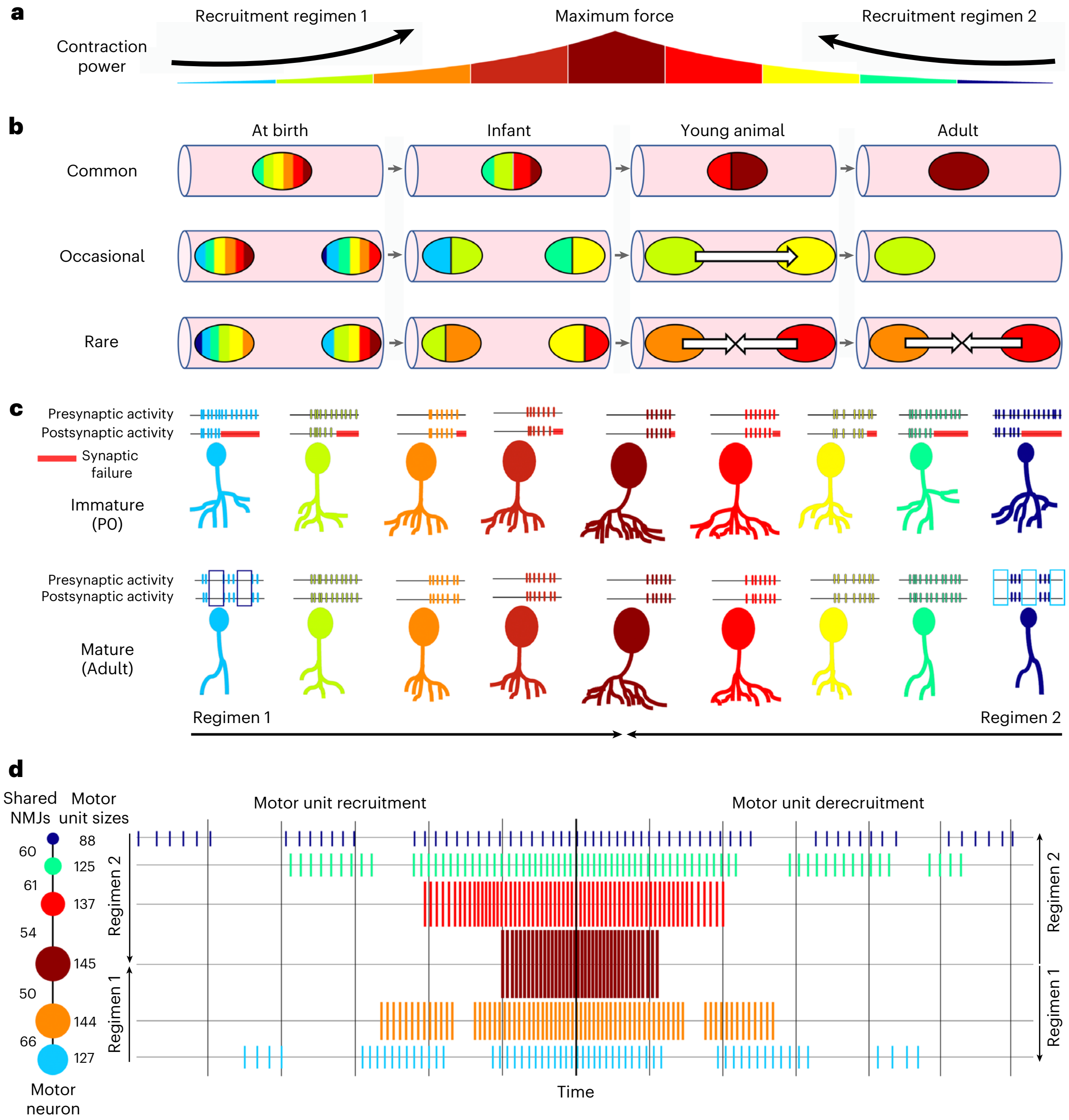

Fig. 7 | The factors that bring about the refinement in the neuromuscular connectome. **a**, One important factor is the tendency for motor axons to be recruited in a fixed order from the small motor units to larger ones as muscle force increases. **b**, This order explains the three main outcomes for the innervation of muscle fibers at birth: most commonly, large motor units outcompete small motor units at the same NMJ; occasionally, muscle fibers with two NMJs usually favor the NMJ with the axon recruited first, the other junction being eliminated; rarely, the similar activity patterns and large distance between NMJs give rise to the stable maintenance of both NMJs on the same muscle fiber. **c**, All motor units trim branches during this refinement. However, the axons that are most persistently active, that is, those recruited earliest, may need to trim more branches because neuronal resources are limited and must be allocated either to neural activity (in the first-recruited tonic motor units) or to maintaining axonal branching and synaptic machinery (in the last-recruited fast motor units). At early ages, the larger tonic motor units are ineffective at driving postsynaptic muscle fibers to threshold; hence, presynaptic activity is inefficient. After branches are trimmed, the tonic axons consistently drive postsynaptic activity. Fatigue may be prevented by alternating different tonic motor units to maintain tone (light and dark blue boxes in **c**). **d**, Putative neural activity pattern of motor neurons at P6–P9 during recruitment and derecruitment. The small neurons (blue-green tinted spikes) at the top and bottom exhibit tonic activity with a lower interspike interval during muscle activation and the large neurons (red-orange tinted spikes) produce shorter-lived high-frequency bursts. Neurons that are next to each other share many muscle fibers and are expected to exhibit more similar activity patterns, allowing them to co-innervate the same NMJs for longer periods than neurons that are far from each other and share only a few NMJs. The alternation in the activity between the top and bottom blue motor neurons is compatible with data on 'motor unit rotation'[44]. The area of the circles is a rough representation of the relative size of the motor units.

same muscle fiber either within a junction (albeit temporarily) or at distant junctions on the same fiber. This similarity supports the idea that NMJ loss and synapse elimination within NMJs are driven by the same patterned-activity-dependent process.

Previous work has highlighted the degree of nonsynchrony required for synaptic competition between axons converging at individual reinnervated multiply innervated NMJs[9,47]. Here we show that timing also plays a role when the competition is between distant synaptic sites. This action-at-a-distance activity effect also explains synapse distribution in other systems. In snakes, adult tonic muscle fibers that cannot elicit APs maintain both multiple NMJs on the same muscle fiber and multiple innervation at each junction, while

AP-generating muscle fibers in the same muscle have only one singly innervated NMJ each[48]. In amphibian MEFs, nearby NMJs have lower synaptic efficacy compared with those farther apart[49], consistent with synaptic weakening when junctions are close. This same idea may also provide insight into the relative absence of excitatory synapses on neuronal somata in peripheral ganglion cells in rodents[50], and, more speculatively, the paucity of excitatory synapses on pyramidal cell somata in the cerebral cortex[51].

Rank ordering of synaptic connections as a consequence of the rank ordering of axonal activity

Given the orderly recruitment of motor neurons[10,42], axons coexisting at the two sites on a MEF should be near each other in the recruitment order. If the same axon innervates more than one MEF it is possible for the MEFs to interconnect neurons to form a network that approximates the recruitment order. In one adult muscle, we indeed found a continuous network connecting 11 motor axons (Fig. 1) to all 16 MEFs in the muscle. The same gapless network motif was even more striking for axons sharing multiply innervated NMJs in a number of muscles between P6 and P9 (Figs. 4a and 5a,b and Extended Data Fig. 6). In all seven muscles we found evidence of a contiguous network where neurons shared most junctions with their nearest neighbors which may reflect recruitment order. We interpret the gapless connectivity as consistent with the patterned-activity-dependent principle described above, positing that for both inter- and intrajunctional connectivity, synaptic release sites are maintained longest (potentially permanently) when their activity pattern is closely matched to the prevailing activity pattern on the same muscle fiber. Indeed, even when only one axon remains at an NMJ, its long-term stability likely reflects the near-synchronous neurotransmitter release at each of its many release sites. In this sense, synapse elimination ends not because a developmental window closes, but rather because the neural circuit has reached a stable state. Consistent with this idea, destabilizing this synchrony induces synapse elimination as occurs following incomplete nerve regeneration to NMJs[52], blocking some postsynaptic receptor sites[7] or local synapse degradation in old age[53].

Connectomic reconstructions of all the motor units in muscles reveal a rank-ordering arrangement of motor axons that we ascribe to the position of motor units in the recruitment order. Interestingly, both in the adult and developmental connectomes, this recruitment order can be traversed along more than one path converging on the largest, last-recruited unit (Figs. 1h and 5b and Supplementary Fig. 4). In both an adult MEF network and some of the mid-development networks, we see that the smallest units, which are likely innervating slow, tonic, early-recruited motor units, occupy different ends of the linear order, while the largest units are situated near the center. This ordering suggests that muscle fiber recruitment might begin at one or the other smallest motor units. Multiple recruitment paths are not the way the Henneman size principle is ordinarily described[10] but previous physiological evidence for the principle was limited to a subset of axons innervating a muscle, for technical reasons. Connectomic analysis, by definition, surveys all the axons innervating a muscle. The notion of multiple recruitment paths is compatible with the previous physiological data, but not with the oft-stated assertion that all motor units are part of a single recruitment order. One way to have multiple recruitment regimens in a muscle is if there is alternation or 'rotation and/or substitution' of motor units in recruitment to mitigate fatigue of the frequently used tonic motor axons and their muscle fibers. This alternation could allow the firing of one recruitment order to transiently suppress the other (Fig. 7c,d). Indeed, electromyography recordings show that early-recruited tonic motor units alternate their activity, consistent with cross-inhibition[43,44]. The consistency of these physiological and connectivity results suggests that the wiring diagram is an anatomical record of the activity patterns that became manifest during development, an imprint of which axons fired together and which fired out-of-phase, throughout development, owing to activity-dependent rules for circuit refinement.

The developmental rearrangements related to synapse elimination can have three different outcomes (Fig. 7b). It appears that the largest motor unit, which is recruited last, has the advantage during synapse elimination in an NMJ (hence it is the largest motor unit), but the axon that is recruited first has the advantage for interjunctional competition.

Why does the axon that is recruited last succeed in outcompeting other axons co-innervating the same NMJ? Previous analysis suggested that the total synaptic resources of a neuron are limited, and the amount of neurotransmitter released at a synapse is adversely affected by both the size of the motor unit and the frequency of release[54]. This view aligns with experimental findings that inactive axons can have large motor units[20]. In the adult, all motor units are optimized for efficacious synapses, meaning that large motor units must fire relatively infrequently to avoid running out of resources, and highly active motor units must be relatively small to maintain their release characteristics. This requirement may mean that during development the first-recruited (that is, most active) motor neurons (see blue neurons in Fig. 7c) do not consistently release enough neurotransmitter molecules to bring their postsynaptic targets to threshold. This failure of synaptic transmission, owing to their high frequency of firing and larger-than-adult-sized motor units, means they will lose competitions to more reliable synaptic inputs. Conversely, the large motor units (red motor neurons in Fig. 7c) convey their activity to their postsynaptic targets more reliably owing to their lower frequency of firing. With the advent of voltage-sensitive dyes that can detect subthreshold activity[55–57], coupled with imaging the developing neuromuscular connectome (in this paper), it may be possible to clarify the role of each neuron's activity in mediating synapse reorganization in muscle.

Prenatal activity's role

Our results demonstrate the profound trimming of motor neuron connectivity in early postnatal life (Figs. 1c and 6c and Extended Data Figs. 1 and 7). Despite the high complexity of the wiring diagram at birth, this early connectome already prefigures the adult connectivity pattern. This early postnatal patterning may be explained by the effects of prenatal motor activity setting in motion the pruning process. Indeed, at birth, ~40% of an all-to-all connectivity pattern is present, perhaps because many connections are already removed. In this context, prenatal motor activity may play an important role in initiating the processes that lead to the final neural connectivity pattern in adult muscle. Importantly, however, the continued refinement of the newborn connectome cannot have occurred by random synapse elimination. This is evident because of the highly structured connectivity at 1 week of age. Moreover, newborns have many large motor units and relatively few small motor units, whereas adults have many small motor units and only a few large motor units (Figs. 1d and 6b and Extended Data Fig. 1b). Our attempts to predict the adult pattern from the newborn pattern by stochastic pruning of connections failed (Extended Data Fig. 10 and Supplementary Fig. 11). Thus, selective synapse elimination mechanisms in postnatal life must play a central role in establishing the particular sizes of the motor units that are used for graded recruitment of tension in muscle (reviewed in Fig. 7c).

The pervasive role of recruitment in neural circuitry

In the motor system, the ordered recruitment of neuronal activity during muscle fiber contraction is a central feature of muscle action. Based on the results presented, we infer that this property emerges over development by the gradual homogenization of the neuronal activity experienced by each muscle fiber, as the differences in recruitment time among neurons converging onto the same muscle fiber become progressively smaller due to pruning of activity outliers.

In muscles, most of the developmental overlapping network organization subsides when muscle fibers become singly innervated (the only remnant is the ordered connectivity of the few remaining MEFs). However, in other parts of the peripheral nervous system, target cells also undergo synapse elimination but remain multiply innervated in adulthood[58]. Interestingly, the sympathetic nervous system possesses an overlapping, rank-ordered motif similar to what we find in muscles. Individual ganglion cells are innervated by contiguous subsets of the rostro-caudally ordered spinal cord segments that supply innervation to each ganglion[59,60]. The purpose is apparently to drive sympathetic end-organs in different regions of body space by input from different spinal cord levels[61]. Analogous to the recruitment order in muscle, sympathetic responses such as piloerection likely occur as propagating waves rather than synchronously (for example, 'chills run down one's spine'). Recruitment waves of activity may underlie similar-appearing connectivity patterns in these two different parts of the nervous system. In an analogous way, retinal waves that link nearby retinal ganglion cell activity could be critical in the development of graded connectivity patterns in the downstream visual system[62–67]. The results described here support the view that a detailed analysis of the structure of a connectome may provide insights into the activity patterns that gave rise to it and hence provide a means of determining the physical engram of previous experiences.

Online content

Any methods, additional references, Nature Portfolio reporting summaries, source data, extended data, supplementary information, acknowledgements, peer review information; details of author contributions and competing interests; and statements of data and code availability are available at https://doi.org/10.1038/s41593-026-02344-7.

References

1. Purves, D. & Lichtman, J. W. Elimination of synapses in the developing nervous system. *Science* **210**, 153–157 (1980).
2. Sanes, D. H., Reh, T. A. & Harris, W. A. *Development of the Nervous System* (Elsevier, 2005).
3. Thompson, W. Synapse elimination in neonatal rat muscle is sensitive to pattern of muscle use. *Nature* **302**, 614–616 (1983).
4. Brown, M. C., Jansen, J. K. & Van Essen, D. Polyneuronal innervation of skeletal muscle in new-born rats and its elimination during maturation. *J. Physiol.* **261**, 387–422 (1976).
5. Lichtman, J. W. & Colman, H. Synapse elimination and indelible memory. *Neuron* **25**, 269–278 (2000).
6. Walsh, M. K. & Lichtman, J. W. In vivo time-lapse imaging of synaptic takeover associated with naturally occurring synapse elimination. *Neuron* **37**, 67–73 (2003).
7. Balice-Gordon, R. J. & Lichtman, J. W. Long-term synapse loss induced by focal blockade of postsynaptic receptors. *Nature* **372**, 519–524 (1994).
8. Turney, S. G. & Lichtman, J. W. Reversing the outcome of synapse elimination at developing neuromuscular junctions in vivo: evidence for synaptic competition and its mechanism. *PLOS Biol.* **10**, e1001352 (2012).
9. Favero, M., Busetto, G. & Cangiano, A. Spike timing plays a key role in synapse elimination at the neuromuscular junction. *Proc. Natl Acad. Sci. USA* **109**, E1667–E1675 (2012).
10. Henneman, E. Relation between size of neurons and their susceptibility to discharge. *Science* **126**, 1345–1347 (1957).
11. Carrascal, L., Nieto-González, J. L., Torres, B. & Nunez-Abades, P. Diminution of voltage threshold plays a key role in determining recruitment of oculomotor nucleus motoneurons during postnatal development. *PLOS ONE* **6**, e28748 (2011).
12. Walton, K. & Fulton, B. P. Ionic mechanisms underlying the firing properties of rat neonatal motoneurons studied in vitro. *Neuroscience* **19**, 669–683 (1986).
13. Clamann, H. P. Motor unit recruitment and the gradation of muscle force. *Phys. Ther.* **73**, 830–843 (1993).
14. Milner-Brown, H. S., Stein, R. B. & Yemm, R. The orderly recruitment of human motor units during voluntary isometric contractions. *J. Physiol.* **230**, 359–370 (1973).
15. Tapia, J. C. et al. Pervasive synaptic branch removal in the mammalian neuromuscular system at birth. *Neuron* **74**, 816–829 (2012).
16. Lu, J., Tapia, J. C., White, O. L. & Lichtman, J. W. The interscutularis muscle connectome. *PLOS Biol.* **7**, e1000032 (2009).
17. Frontera, W. R. & Ochala, J. Skeletal muscle: a brief review of structure and function. *Calcif. Tissue Int.* **96**, 183–195 (2015).
18. Rafuse, V. F., Pattullo, M. C. & Gordon, T. Innervation ratio and motor unit force in large muscles: a study of chronically stimulated cat medial gastrocnemius. *J. Physiol.* **499**, 809–823 (1997).
19. Krivickas, L. S., Dorer, D. J., Ochala, J. & Frontera, W. R. Relationship between force and size in human single muscle fibres: muscle fibre size and force. *Exp. Physiol.* **96**, 539–547 (2011).
20. Callaway, E. M., Soha, J. M. & Van Essen, D. C. Competition favouring inactive over active motor neurons during synapse elimination. *Nature* **328**, 422–426 (1987).
21. Callaway, E. M., Soha, J. M. & Van Essen, D. C. Differential loss of neuromuscular connections according to activity level and spinal position of neonatal rabbit soleus motor neurons. *J. Neurosci.* **9**, 1806–1824 (1989).
22. Personius, K. E. & Balice-Gordon, R. J. Loss of correlated motor neuron activity during synaptic competition at developing neuromuscular synapses. *Neuron* **31**, 395–408 (2001).
23. Wyatt, R. M. & Balice-Gordon, R. J. Activity-dependent elimination of neuromuscular synapses. *J. Neurocytol.* **32**, 777–794 (2003).
24. Balice-Gordon, R. J. & Lichtman, J. W. In vivo observations of pre- and postsynaptic changes during the transition from multiple to single innervation at developing neuromuscular junctions. *J. Neurosci.* **13**, 834–855 (1993).
25. Callaway, E. M. & Van Essen, D. C. Slowing of synapse elimination by α-bungarotoxin superfusion of the neonatal rabbit soleus muscle. *Dev. Biol.* **131**, 356–365 (1989).
26. Buffelli, M. et al. Genetic evidence that relative synaptic efficacy biases the outcome of synaptic competition. *Nature* **424**, 430–434 (2003).
27. Lomo, T. & Rosenthal, J. Control of ACh sensitivity by muscle activity in the rat. *J. Physiol.* **221**, 493–513 (1972).
28. Katz, B. & Kuffler, S. W. Multiple motor innervation of the frog's sartorius muscle. *J. Neurophysiol.* **4**, 209–223 (1941).
29. McComas, A. J., Kereshi, S. & Manzano, G. Multiple innervation of human muscle fibers. *J. Neurol. Sci.* **64**, 55–64 (1984).
30. Lateva, Z. C., McGill, K. C. & Johanson, M. E. Electrophysiological evidence of adult human skeletal muscle fibres with multiple endplates and polyneuronal innervation. *J. Physiol.* **544**, 549–565 (2002).
31. Lateva, Z. C., McGill, K. C. & Elise Johanson, M. The innervation and organization of motor units in a series-fibered human muscle: the brachioradialis. *J. Appl. Physiol.* **108**, 1530–1541 (2010).
32. Kupa, E. J., Roy, S. H., Kandarian, S. C. & De Luca, C. J. Effects of muscle fiber type and size on EMG median frequency and conduction velocity. *J. Appl. Physiol.* **79**, 23–32 (1995).
33. Banks, Q. et al. Optical recording of action potential initiation and propagation in mouse skeletal muscle fibers. *Biophys. J.* **115**, 2127–2140 (2018).
34. Katz, B. & Miledi, R. Propagation of electric activity in motor nerve terminals. *Proc. R. Soc. Lond. B* **161**, 453–482 (1965).
35. Katz, B. & Miledi, R. The measurement of synaptic delay, and the time course of acetylcholine release at the neuromuscular junction. *Proc. R. Soc. Lond. B* **161**, 483–495 (1965).

36. Waxman, S. G. & Bennett, M. V. Relative conduction velocities of small myelinated and non-myelinated fibres in the central nervous system. *Nat. New Biol.* **238**, 217–219 (1972).
37. Datyner, N. B. & Gage, P. W. Phasic secretion of acetylcholine at a mammalian neuromuscular junction. *J. Physiol.* **303**, 299–314 (1980).
38. Del Vecchio, A. et al. You are as fast as your motor neurons: speed of recruitment and maximal discharge of motor neurons determine the maximal rate of force development in humans. *J. Physiol.* **597**, 2445–2456 (2019).
39. Livet, J. et al. Transgenic strategies for combinatorial expression of fluorescent proteins in the nervous system. *Nature* **450**, 56–62 (2007).
40. Tsuriel, S., Gudes, S., Draft, R. W., Binshtok, A. M. & Lichtman, J. W. Multispectral labeling technique to map many neighboring axonal projections in the same tissue. *Nat. Methods* **12**, 547–552 (2015).
41. Buffelli, M., Busetto, G., Cangiano, L. & Cangiano, A. Perinatal switch from synchronous to asynchronous activity of motoneurons: link with synapse elimination. *Proc. Natl Acad. Sci. USA* **99**, 13200–13205 (2002).
42. Zajac, F. E. & Faden, J. S. Relationship among recruitment order, axonal conduction velocity, and muscle-unit properties of type-identified motor units in cat plantaris muscle. *J. Neurophysiol.* **53**, 1303–1322 (1985).
43. Westgaard, R. H. & de Luca, C. J. Motor unit substitution in long-duration contractions of the human trapezius muscle. *J. Neurophysiol.* **82**, 501–504 (1999).
44. Bawa, P. & Murnaghan, C. Motor unit rotation in a variety of human muscles. *J. Neurophysiol.* **102**, 2265–2272 (2009).
45. Sanes, J. R. & Lichtman, J. W. Induction, assembly, maturation and maintenance of a postsynaptic apparatus. *Nat. Rev. Neurosci.* **2**, 791–805 (2001).
46. Lin, W. et al. Distinct roles of nerve and muscle in postsynaptic differentiation of the neuromuscular synapse. *Nature* **410**, 1057–1064 (2001).
47. Favero, M., Buffelli, M., Cangiano, A. & Busetto, G. The timing of impulse activity shapes the process of synaptic competition at the neuromuscular junction. *Neuroscience* **167**, 343–353 (2010).
48. Lichtman, J. W., Wilkinson, R. S. & Rich, M. M. Multiple innervation of tonic endplates revealed by activity-dependent uptake of fluorescent probes. *Nature* **314**, 357–359 (1985).
49. Haimann, C., Mallart, A., Ferré, J. T. & Zilber-Gachelin, N. F. Patterns of motor innervation in the pectoral muscle of adult *Xenopus laevis*: evidence for possible synaptic remodelling. *J. Physiol.* **310**, 241–256 (1981).
50. Hume, R. I. & Purves, D. Apportionment of the terminals from single preganglionic axons to target neurones in the rabbit ciliary ganglion. *J. Physiol.* **338**, 259–275 (1983).
51. Shapson-Coe, A. et al. A petavoxel fragment of human cerebral cortex reconstructed at nanoscale resolution. *Science* **384**, eadk4858 (2024).
52. Rich, M. M. & Lichtman, J. W. In vivo visualization of pre- and postsynaptic changes during synapse elimination in reinnervated mouse muscle. *J. Neurosci.* **9**, 1781–1805 (1989).
53. Valdez, G. et al. Attenuation of age-related changes in mouse neuromuscular synapses by caloric restriction and exercise. *Proc. Natl Acad. Sci. USA* **107**, 14863–14868 (2010).
54. Barber, M. J. & Lichtman, J. W. Activity-driven synapse elimination leads paradoxically to domination by inactive neurons. *J. Neurosci.* **19**, 9975–9985 (1999).
55. Hochbaum, D. R. et al. All-optical electrophysiology in mammalian neurons using engineered microbial rhodopsins. *Nat. Methods* **11**, 825–833 (2014).
56. Evans, S. W. et al. A positively tuned voltage indicator for extended electrical recordings in the brain. *Nat. Methods* **20**, 1104–1113 (2023).
57. Abdelfattah, A. S. et al. Sensitivity optimization of a rhodopsin-based fluorescent voltage indicator. *Neuron* **111**, 1547–1563 (2023).
58. Lichtman, J. W. & Purves, D. The elimination of redundant preganglionic innervation to hamster sympathetic ganglion cells in early post-natal life. *J. Physiol.* **301**, 213–228 (1980).
59. Njå, A. & Purves, D. Specific innervation of guinea-pig superior cervical ganglion cells by preganglionic fibres arising from different levels of the spinal cord. *J. Physiol.* **264**, 565–583 (1977).
60. Lichtman, J. W., Purves, D. & Yip, J. W. Innervation of sympathetic neurones in the guinea-pig thoracic chain. *J. Physiol.* **298**, 285–299 (1980).
61. Lichtman, J. W., Purves, D. & Yip, J. W. On the purpose of selective innervation of guinea-pig superior cervical ganglion cells. *J. Physiol.* **292**, 69–84 (1979).
62. Meister, M., Wong, R. O., Baylor, D. A. & Shatz, C. J. Synchronous bursts of action potentials in ganglion cells of the developing mammalian retina. *Science* **252**, 939–943 (1991).
63. Huberman, A. D., Feller, M. B. & Chapman, B. Mechanisms underlying development of visual maps and receptive fields. *Annu. Rev. Neurosci.* **31**, 479–509 (2008).
64. Kirkby, L. A., Sack, G. S., Firl, A. & Feller, M. B. A role for correlated spontaneous activity in the assembly of neural circuits. *Neuron* **80**, 1129–1144 (2013).
65. Assali, A., Gaspar, P. & Rebsam, A. Activity dependent mechanisms of visual map formation-from retinal waves to molecular regulators. *Semin. Cell Dev. Biol.* **35**, 136–146 (2014).
66. Thompson, A., Gribizis, A., Chen, C. & Crair, M. C. Activity-dependent development of visual receptive fields. *Curr. Opin. Neurobiol.* **42**, 136–143 (2017).
67. Tiriac, A., Smith, B. E. & Feller, M. B. Light prior to eye opening promotes retinal waves and eye-specific segregation. *Neuron* **100**, 1059–1065 (2018).

Publisher's note Springer Nature remains neutral with regard to jurisdictional claims in published maps and institutional affiliations.

Open Access This article is licensed under a Creative Commons Attribution-NonCommercial-NoDerivatives 4.0 International License, which permits any non-commercial use, sharing, distribution and reproduction in any medium or format, as long as you give appropriate credit to the original author(s) and the source, provide a link to the Creative Commons licence, and indicate if you modified the licensed material. You do not have permission under this licence to share adapted material derived from this article or parts of it. The images or other third party material in this article are included in the article's Creative Commons licence, unless indicated otherwise in a credit line to the material. If material is not included in the article's Creative Commons licence and your intended use is not permitted by statutory regulation or exceeds the permitted use, you will need to obtain permission directly from the copyright holder. To view a copy of this licence, visit http://creativecommons.org/licenses/by-nc-nd/4.0/.

© The Author(s) 2026

Methods

Sample acquisition and preparation of newborn tissue for serial-section SEM

Thy1-YFP16 mice[68] were maintained, bred and housed according to the guidelines of Harvard University's Faculty of Arts and Sciences Institutional Animal Care and Use Committee (FAS IACUC), on a 12-h:12-h light to dark cycle at 22 ± 2 °C and 30–70% relative humidity. Newborn pups (P0) were deeply anesthetized with ketamine–xylazine. The interscutularis muscle was exposed and labeled with 5 μg ml^{-1} Alexa 647-conjugated α-bungarotoxin (α-btx; Thermo Fisher Scientific) for 10 min at room temperature to stain NMJ acetylcholine receptors. Immediately after thoroughly rinsing with 0.1 M phosphate-buffered saline (PBS, pH 7.4; Thermo Fisher Scientific), the interscutularis muscle was immersed in 2% glutaraldehyde (Electron Microscopy Sciences (EMS)) and 2% paraformaldehyde (PFA; EMS) in 0.1 M sodium cacodylate buffer (pH 7.4) for 6 h at 4 °C. Under a fluorescent dissecting scope (Leica), the interscutularis muscle was isolated and trimmed to include the entire endplate band and ~1 mm of the posterior auricular nerve. The sample was imaged using a Zeiss LSM-710 confocal microscope with a Plan-Neofluar ×10, 0.3 numerical aperture (NA) objective. YFP and Alexa 647 were excited by 514-nm and 633-nm lasers, respectively. Confocal imaging captured the nerve's rough contour of innervation, assisting further electron microscope image processing. Tiled stacks of the entire endplate band were scanned for YFP and Alexa 647 simultaneously at resolutions of 0.923 μm, 0.923 μm and 3.017 μm for the x, y and z dimensions, respectively. After imaging, the sample was postfixed with 2% glutaraldehyde and 2% PFA in sodium cacodylate buffer (0.1 M, pH 7.4) at 4 °C for 12 h, and processed for EM[69]. Briefly, the sample was contrasted with ROTO (reduced osmium tetroxide–thiocarbohydrazide–osmium tetroxide) and dehydrated with graded ethanol concentrations (20%, 50%, 70%, 80%, 90% and 100%; 15 min each) and propylene oxide (15 min twice). Finally, the sample was immersed in mixtures of propylene oxide and Plain Resin (Nisshin EM) in ratios of 3:1 (30 min), 1:1 (1 h) and 1:3 (3 h), followed by infiltration with pure Plain Resin for 12 h. After replacing the resin at least four times, the sample was embedded in beam capsules and cured in an oven at 50 °C for 24 h and 70 °C for 4 d.

Sample sectioning for ssSEM

The resin block surface was first trimmed to a rectangle. The corners were then trimmed to form an arrow-point on each end, creating a six-sided polygon, using a 3-mm ultratrim diamond knife (Diatome) and a UC6 ultramicrotome (Leica). The fibers were aligned with the length of the rectangle and sectioned perpendicular to their direction to reduce sectioning compression. Serial sections, 60 nm thick, were cut with a 45° ultra diamond knife (Diatome) and collected using the automated tape ultramicrotome (ATUM) system[70]. Sections were cut at 0.3 mm s^{-1} and collected onto carbon-coated Kapton tape. A total of 3,232 serial sections were collected. The first 2,315 sections contained muscle tissue and the innervating nerve. The subsequent 917 sections contained only the nerve, with no muscle.

Wafer fabrication and mapping for ssSEM

The tape holding the sections was cut into strips with a razor blade between collected sections and adhered with 25.4-mm-wide double-sided conductive carbon adhesive tape (Ted Pella) onto 100-mm diameter circular wafers (University Wafers). A total of 3,232 sections were distributed across 25 wafers. To enhance the signal from cell membranes, each wafer was plasma-treated for 30 s (operating pressure of 1×10^{-1} mb, plasma current of 15 mA) to increase hydrophilicity. The wafers were immediately stained with 4% uranyl acetate for 3 min, rinsed with ddH$_2$O for 30 s (10 times), air-dried, stained with 3% lead citrate (Leica UltroStain II) for 3 min, rinsed and air-dried as before, and stored under vacuum. Each wafer was mounted on a metal wafer holder with fiducials for high-resolution imaging using a multibeam scanning electron microscope (MultiSEM 505, Zeiss). A low-resolution (3.57 μm per pixel) optical image was acquired from each wafer to identify the position of each section relative to the wafer holder fiducials[71]. A six-sided polygonal region of interest (ROI) was defined and superimposed onto each section in the optical image of each wafer using the Zen software package (Zeiss Microscopy) to target high-resolution imaging with the MultiSEM 505.

ssSEM image acquisition

The first 18 wafers contained the interscutularis muscle and nerve fibers innervating the muscle. These sections were imaged using a multibeam scanning electron microscope, which employs 61 electron beams to scan 61 overlapping rectangular regions simultaneously[72], producing 61 image tiles. These 61 tiles form one large hexagonal image known as a multi-field-of-view (mFoV). Once one mFoV was acquired, the multibeam scanning electron microscope stage moved to an adjacent site to acquire another mFoV. All images were scanned at a resolution of 4 nm per pixel, with a tile overlap (within mFoV) of 0.5 μm and a between-mFoV overlap of 4%. Each ROI was imaged with a landing energy of 1.5 kV, each scanning beam at 570 pA and a dwell time of 3.2 μs per pixel. Brightness and contrast for each ROI were set to maximize the dynamic range of the images by optimizing the histogram spread of image gray levels without clipping. Before imaging each ROI, the MultiSEM was programmed to determine the optimal focus height and stigmation settings at 'focus support points' (FSPs) within the section. If this procedure failed at more than 25% of the FSPs, the ROI was not acquired, and the procedure was restarted with new FSPs added and failed FSPs removed or moved. Once successful at 75% or more FSPs, Delaunay triangulation was used to interpolate a topological map of the ROI, guiding the autofocus of the MultiSEM during imaging. The last seven wafers with sections containing only nerve fibers were imaged using a single electron beam ZEISS Sigma. These images were scanned at a resolution of 4 nm per pixel, with a landing energy of 1.7 kV at 1 nA, and a dwell time of 200 ns per pixel.

Image stitching and alignment of the newborn ssSEM dataset

Stitching and alignment of the dataset were challenging because of the large spatial section area, sparse image features in many tiles and sections, the arc-like tissue geometry and local wrinkles. The overall workflow was similar to that in ref. 73, with each step parallelized over image tiles and sections. For stitching, approximate tile locations from the MultiSEM stage coordinates were used to identify overlaps between neighboring tiles. Overlapping regions were contrast-enhanced with CLAHE, particularly in low-texture regions, matched using ORB features[74], filtered for outliers with RANSAC[75] under rigid-transformation constraints and then used to optimize tile position and rotation by minimizing correspondence error. For three-dimensional (3D) alignment, coarse feature matching was performed between neighboring sections up to two sections apart using SimpleBlobDetector and SIFT descriptors[76]; the blob detector identified dark lipid-like features appearing in similar locations across consecutive sections. These coarse matches were used to guide fine patch-based cross-correlation matching on a triangular mesh, followed by 3D elastic optimization to minimize cross-section mismatch while preserving the 2D structure of individual sections.

Semantic and instance segmentation of the newborn ssSEM dataset

NMJ identification. Three annotators exhaustively searched for NMJs by scrolling through the volume in VAST[77] at a low mip-level, identifying axon bundles and presynaptic vesicle-filled swellings. Three independent strategies were adopted for NMJ identification: one annotator followed fibers along their entire length, another annotator searched for axon terminals and a third annotator extracted candidate locations based on the confocal stack stained with α-btx to identify acetylcholine receptor sites.

Muscle fiber reconstruction. An expert annotator enumerated and seeded all myofibers intersecting the right side of the volume by scrolling through the z axis, identifying the rightmost extremity of each myofiber, naming it and segmenting part of the fiber to aid the visual search for additional fibers. This resulted in the identification of 208 muscle fibers, which were then skeletonized by a second annotator. After the initially seeded fibers were saturated, the remaining 32 fibers were identified by backtracking from NMJs not yet associated with a skeletonized fiber and by an exhaustive search for missing fibers in the middle plane of the dataset by an independent annotator. These 32 fibers were secondary fibers that did not reach the right side of the dataset ($n = 26$; Supplementary Fig. 12), damaged fibers ($n = 5$) or peripheral fibers exiting the volume more medially than the initial imaging boundary ($n = 3$). Additional myofiber-like cellular structures were classified as myoblasts based on their lack of sarcomere structure, shorter extent and irregular sarcolemma. Interestingly, all secondary fibers possessed an NMJ close to that of their morphologically associated primary fiber, as previously reported[78].

Volumetric instance segmentation of muscle fibers. To obtain a volumetric representation of the muscle fibers, we trained a neural network to detect sarcolemma, sarcoplasm and voxels corresponding to neither category, and applied it to the full dataset using mEMbrain[79] to generate voxelwise scores for the three classes. Human annotations were then used as seeds for a 3D watershed algorithm after Gaussian smoothing of the probability maps. Postprocessing removed object voxels far from the initially annotated regions, applied majority voting across sections and used spherical filling around annotated regions that were not fully expanded.

Myonuclei reconstruction. The polynuclear nature of muscle fiber cells is thought to control transcriptional activity in segmented domains of cytoplasm surrounding the nuclei. This myonuclear domain varies between fiber types[80] and is inversely associated with the fiber's oxidative capacity[80,81]. In vertebrate skeletal muscle, myonuclei cluster at the muscle fiber endplates near NMJs, forming aggregates of synaptic nuclei with distinctive functions and morphology[82]. Comparing the myonuclear domains of MEFs and SEFs can provide insights into key differences between these fiber types. To approximate the myonuclear domain, defined as (volume of fiber)/(number of nuclei in fiber), we used the following formula: constant × (fiber CSA)/(number of nuclei), assuming fibers maintain a relatively fixed CSA and similar lengths. We reconstructed all synaptic and nonsynaptic myonuclei from 52 randomly selected newborn muscle fibers (25 MEFs and 27 SEFs; 930 nuclei total; Supplementary Fig. 13). One annotator placed skeleton nodes in each nucleus. A neural network trained using mEMbrain[79] classified pixels into nucleoplasm, nuclear membrane and nonnuclear categories. A second annotator then expanded each seeded nucleus using VAST's flood-filling tool[77], leveraging the classified pixels as constraints, with threshold adjustment and human correction where needed to prevent underfilling or overflow across nuclear boundaries. This semiautomatic procedure was several times faster than fully manual annotation. Finally, the nuclei were visualized in 3D and further analyzed.

Sarcomere spacing in MEFs and SEFs. Sarcomere spacing was measured in the newborn EM dataset as the distance between adjacent Z-lines. Consistent with the absence of a clear difference in myonuclear domain between MEFs and SEFs, sarcomere spacing was unimodally distributed and did not differ distinctly between the two fiber classes (Supplementary Fig. 14).

Axon instance segmentation: motor nerve. All axons were enumerated and manually skeletonized from wafer 12 to wafer 25, covering over 1,827 sections. This analysis identified a single fascicle containing nerve cells and Schwann cells, surrounded by perineurium tissue. Low-magnification inspection of the EM suggested no other fascicles projected to the interscutularis muscle. To better estimate the number of distinct axons in this nerve, we identified and analyzed several cross sections of the nerve about 1,000 sections distal to the muscle (approximately 200 µm distal to the muscle fibers). The number of individual axonal cross sections in these slices matched the number of axons identified in the fully reconstructed nerve segment, that is, 21 axons. One axon had a short arborization inside the muscle tissue, without innervating any NMJ. The manually skeletonized axons were then expanded into volumetric 3D reconstructions using mEMbrain[79], with an approach similar to that used for muscle fibers.

Axon instance segmentation: axon bundles. The 21 axons identified in the nerve reconstruction were traced throughout the muscle by seven annotators (three experts and four extensively trained undergraduate students), requiring more than 3,500 annotation hours. The first task was to skeletonize the axonal bundles iteratively through all possible bifurcations using VAST[77]. Once this process was saturated, three annotators began tracing from identified NMJs, connecting anonymous axon segments to identified fascicles. This continued until all axonal branches were either associated with a synapse (the vast majority of cases) or reached specialized zones containing disorganized axonal swellings surrounded by intricate glial processes close to the sarcolemma of a muscle fiber (Supplementary Figs. 15 and 16). The nature of these regions could not be determined definitively, but we hypothesize that they are related to sites of muscle innervation from the embryonic stage and may be associated with early-stage axonal retraction from NMJs.

Sample preparation of Brainbow mice

Transgenic Brainbow animals. To label motor neurons in multiple colors, we initially tried first-generation multicolor transgenic strategies that relied on cytoplasmic expression of fluorescent proteins[39]. These strategies fell short because of limited color separability or low expression early in postnatal life. To achieve early, bright labeling in many colors, we developed new Brainbow lines in which all fluorescent proteins were membrane-tethered (Extended Data Fig. 3). Brainbow and Thy1-YFP16 mice were maintained, bred and housed according to the guidelines of the IACUC, on a 12-h:12-h light to dark cycle at 22 ± 2 °C and 30–70% relative humidity. Because changes in axon caliber alter volume more than surface area, we reasoned that a membrane label might provide brighter and more uniform labeling of the fine neural structures than a cytoplasmic label at the same expression level. To create the multicolor membrane label (Membrane), we generated Brainbow mice in which three fluorescent proteins (eCFP, eYFP and mCherry) were directed to the plasma membrane by an N-terminal palmitoylation tag[83]. We crossed these mice with Hb9^{cre} transgenic mice, which express Cre recombinase postmitotically in motor neurons[84]. In vivo expression of the fluorescent proteins was largely restricted to the plasma membrane, primarily in axons and almost absent from soma and dendrites, likely contributing to increased axonal brightness. Thy1-Membrane-Brainbow animals were generated as described[31] and crossed with Hb9^{cre} animals obtained from Jackson Labs (JAX stock no. 006600). Breeding for the Thy1-Membrane-Brainbow line was discontinued after this study, and the line would need to be regenerated for future research.

Histology (Brainbow). Mice were deeply anesthetized with sodium pentobarbital and perfused transcardially with ice-cold 4% PFA (EMS) in PBS. Muscles were dissected and postfixed in 4% PFA for 30 min at 4 °C with gentle rocking in the dark. Muscles were rinsed in 0.1 M glycine in PBS for 10 min, washed in PBS for 5 min, then incubated for 30 min with 5 µg ml^{-1} Alexa 647-conjugated α-btx (Thermo Fisher Scientific) dissolved in 1% BSA (Sigma-Aldrich) in PBS. Muscles were rinsed again in PBS for 15 min. Finally, tissues were mounted on slides in Vectashield

H-1000 fluorescent mounting media (Vector Laboratories), coverslipped under gentle magnetic pressure, allowed to set overnight at −20 °C, then sealed with nail polish (EMS) and stored frozen at −20 °C. To obtain samples in which all axons could be identified by color, we screened hundreds of animals and selected muscles with at most one or two color redundancies at the muscle entry site. We consistently observed more axon collaterals than colors at the entry site, suggesting that some identical colors reflected distal branching rather than true color redundancy[16]. In seven muscles, identically colored profiles were interpreted as axon collaterals because they never co-innervated the same NMJ, did not have motor unit sizes twice the average size of others and showed similar skewing in partner preferences. These muscles were therefore analyzed as complete color-segmented connectomes (Extended Data Fig. 4): four omohyoid muscles (P6, six axons; P7, nine axons; P7, six axons; P8, five axons) and three forepaw lumbrical muscles (P9, six axons; P8, six axons; P8, six axons).

Imaging of Brainbow samples. Images were acquired on an Olympus FV1000 confocal microscope using the multiple-area time lapse function with 3% overlap between adjacent tiles and either a ×60, 1.4 NA PlanApo or 1.35 NA UPlanSApo oil-immersion objective lens. Image stacks were collected at 1,024 × 1,024 or 800 × 800 frame size and stepped in *z* by 0.37 µm. Samples were excited in two sequential groups to reduce spectral bleed-through: first with the 440- and 633-nm laser lines, then with the 515- and 561-nm lasers. Emission filters for four spectral channels were set as follows: Cerulean, 480/15 nm; EYFP, 535/15 nm; dTomato and mCherry, 600/25 nm; Alexa 647, long-pass 650 nm. Images were typically collected at 2 µs per pixel with either no averaging or Kalman averaging set to 2.

Identification of presynaptic innervation in the confocal Brainbow stacks. To assess the identity of motor axons at each NMJ, each image stack was evaluated in Imaris using local maximum-intensity projections through the *z* axis. The color of each nonoverlapping axonal terminal at or near the synapse was compared with nearby labeled axons in the same volume; when needed, neurites were followed back along their path to inspect less-overlapped regions and associated branches. If color assignment remained uncertain because of overlap or low contrast, the synapse was scored as ambiguous. This occurred in less than 5% of the total NMJs.

Sample preparation of YFP16 mice

Neonatal Thy1-YFP-16 transgenic mice (P1, P3, P5, P10 and P12) and young adults (P30 and P60) were anesthetized by intraperitoneal injection of ketamine–xylazine (0.1 ml per 20 g; Ketaset, Fort Dodge Animal Health). After deep anesthesia, animals were transcardially perfused with 4% PFA (EMS) in 0.1 M PBS (Sigma-Aldrich), pH 7.4. The interscutularis muscle, together with ~1 mm of the posterior auricular nerve, was dissected and postfixed for 1 h in the same fixative. After rinsing in PBS, samples were incubated with Alexa 594-conjugated α-btx (Thermo Fisher Scientific) for 4 h to stain acetylcholine receptors, then washed in PBS (3 × 30 min). Samples were mounted in Vectashield (H-1000, Vector Laboratories). In some samples, Wheat Germ Agglutinin (WGA) conjugated with Alexa 647 (Thermo Fisher Scientific) was used to label muscle fiber contours and the overall muscle vasculature. Samples were imaged on either an Olympus FV1000 or a Zeiss LSM-710 confocal microscope, as described below.

Confocal imaging of the developmental and adult samples

We imaged whole-mounted neonatal and adult mouse muscles using Zeiss LSM-710 (Carl Zeiss Microscopy) and Olympus FV1000 (Olympus Scientific Solutions Americas) laser-scanning confocal microscopes. These systems were equipped with a motorized stage, high-numerical-aperture oil-immersion objectives (Zeiss Plan-APOCHROMAT ×63/1.4; Olympus UPlanFL N ×40/1.3 and Olympus UPlanSApo N ×60/1.35), and spectral channels for fluorescence detection. The Zeiss and Olympus systems operated with ZEN 2010 and FV10-ASW 4.1 software, respectively, with optional modules for tiled image acquisition (Zeiss: LSM StitchArt; Olympus: multiple-area time lapse). We used a multiband primary dichroic filter to reflect the laser lines needed to excite YFP, Alexa 594 and Alexa 647 (514.5 nm, 561 nm and 633 nm, respectively). For each muscle (P1 to P60), we acquired tiled stacks of the entire endplate band, simultaneously scanning YFP and Alexa 647 and sequentially scanning Alexa 594. The voxel size was isotropic in *x*, *y* and *z* (for example, P1: 0.31 µm, P10: 0.42 µm and P30: 0.83 µm) to facilitate orthogonal- and off-axis slicing in subsequent analysis for mapping NMJs to muscle fibers. The Zeiss tiled datasets were stitched using the LSM StitchArt module. The Olympus tiled datasets were stitched in Fiji[85] using the Grid/Collection stitching plugin[86]. For P60 interscutularis muscle, we also imaged YFP at very high resolution on the Olympus system using the ×60 objective (0.138 µm per pixel in *xy* and 0.2 µm in *z*). The high-resolution single-channel image volume enabled tracing of the full arbor of each YFP-filled axon of the motor input, facilitating the reconstruction of the muscle connectome when combined with the corresponding lower-resolution multichannel image volume.

Reconstruction of muscle fibers and axon arbors and NMJs from the confocal stacks

Muscle fibers, NMJs and MEFs. All confocal stacks were manually annotated by two expert annotators. For the P0, P3, P5, P10, P12, P30 and P60 samples, muscle fibers were counted in two planes perpendicular to the fiber axis, located at approximately one-third and two-thirds of the muscle volume along its longitudinal axis. In all samples, the two counts agreed within ~5 fibers. For P0–P5, the two counts were averaged to estimate the number of muscle fibers in each volume. For P10, P12, P30 and P60, muscle fibers were manually reconstructed, except for one sample that was automatically reconstructed using mEMbrain[79] and manually proofread. NMJs were identified in VAST[77], from 3D renderings of the red (α-btx) and green (YFP16) channels as volumetric structures with stereotypic endplate morphology. At earlier ages (P0–P5), all high-intensity red-channel regions were added to the candidate list. Because all identified NMJs were located near axonal bundles, noisy red-channel aggregates far from the axonal tree were excluded. Each candidate NMJ was then verified in the 2D stack in transverse orientation by confirming the convexity of the α-btx endplate perimeter around the corresponding muscle fiber (WGA channel).

The difference between the number of identified NMJs and the number of identified muscle fibers provided an estimate of the number and proportion of MEFs in each sample. In P10–P60, we also directly classified each muscle fiber as multiple-endplate or single-endplate by animating the 2D stack along the longitudinal axis in VAST. The two methods agreed in the vast majority of cases. When small discrepancies arose (never more than ~5 fibers), the procedure was repeated until the source of the discrepancy was identified.

Axon tracing. Axonal arbors in two adult interscutularis muscles (P60) were traced in VAST[77] by one expert annotator and verified by a second. Each annotator focused on a different part of the dataset, facilitated by very-high-resolution YFP-based confocal images (138 nm per pixel). The most efficient strategy was to trace axons in transverse sections, often using orthogonal plane annotation in VAST. When ambiguities arose, the two annotators reconciled their interpretations, sometimes postponing decisions until neighboring axons had been reconstructed. In all cases, this led to an unambiguous solution.

Muscle fiber CSA measurement. CSAs were measured by reslicing volumes orthogonal to each fiber's long axis and annotating the fiber cross section in that plane; motor-unit 'force' was the sum of fiber CSAs. Classic reconstructions show near-invariant caliber through the muscle belly (<5% CSA variation across the central 80–90% of length), with taper confined to the distal ~1 mm at the myotendinous junction[87–89]. In mouse interscutularis, fibers maintain constant CSA up to blunt insertions[16,90]. We estimated the single-section CSA error distribution from volumetric reconstructions of all 213 fibers in one interscutularis muscle and used this error model to perturb single-section CSAs across all muscles in our Monte Carlo analysis ('Deriving *P* values under the assumption of noisy CSA measurements').

Statistical tools and analysis

Linear order of axons. Whether motor neuron innervation of muscle fibers is initially random or specific has been the subject of theoretical study[91]. A key idea is that synapse elimination outcomes at NMJs may depend in part on the developmental history of the participating axons, including their opportunity to innervate particular junctions. In this framework, the motor system may begin with an excessively dense, approximately random innervation pattern to ensure that each NMJ initially receives at least one synaptic input during subsequent elimination[91].

To assess the randomness of the innervation pattern, we calculated for each axon pair the probability of sharing a given number of muscle fiber targets under a null model in which axons target junctions independently and with equal probability. In the newborn interscutularis muscle, all but one axon arborized across nearly the full longitudinal axis of the muscle and innervated NMJs in both distal and proximal regions relative to the muscle entry point. Because equal likelihood of targeting NMJs does not guarantee true independence between nearby targets, we compared each connectome with random connectomes in which an axon innervating *K* muscle targets selects uniformly among subsets of *K* muscle fibers. These random connectomes provide useful statistical baselines, although they do not capture geometric constraints such as axon trajectory, branching pattern or intervening tissue, which may also influence connectivity during development.

In our model, the connection between two axons is defined by the extent to which their shared number of muscle fiber targets exceeds what would be expected under a random innervation model. Specifically, for two axons with N_1 and N_2 targets, respectively, we calculated the probability of observing *S* shared targets, given *M* equally likely potential innervation sites.

$$P_{\text{share}}(S') = P\big(\text{axons with } N_1 \text{ and } N_2 \text{ targets share exactly } S' \text{ targets} \mid M \text{ possible targets}\big)$$

For two axons sharing *S* targets, we summed the probabilities $P_{\text{share}}(S')$ for $S' \geq S$, which is the probability to observe the number of shared targets or more under the null hypothesis.

$$P_{\text{share}}(S \text{ or more}) = P_{\text{share}}(S) + P_{\text{share}}(S+1) + \ldots + P_{\text{share}}(M)$$

Similarly, we also computed the probability P_{avoid} by considering the number of targets that are not innervated by each axon and the number of targets that are jointly not innervated by the two axons (the complement of the overlap and motor unit sizes).

In this process, we generate networks of probabilities among all pairs of motor axons. Consider, for instance, axons 17, 19 and 21, which form a sub-network as shown in Supplementary Fig. 17. Out of 240 muscle fiber targets, axon 17 innervates 93 fibers (an innervation ratio of approximately 39%), while axon 21 innervates 90 fibers (approximately 38%). Under a model of equal likelihood and independent innervation, one would expect an axon to innervate another's targets at the same rate as it innervates the entire muscle. However, the observed 54 shared targets between axons 17 and 21 account for about 58% and 60% of their respective total targets. The probability of observing this number of shared targets (or more) for motor units of sizes 93 and 90, out of 240 potential targets and assuming independent innervation, is approximately 3.87×10^{-8} (ref. 92). We used P_{share} and P_{avoid} as normalized measures of whether the observed overlap between two axons was consistent with independent innervation, accounting for both motor unit size and the total number of available targets. These values were then used to quantify connection strength in the empirical connectomes and to compare them with random connectomes by Monte Carlo methods (see below).

We also asked whether pairwise tendencies to share or avoid the same targets reflect a broader pattern in the axonal network. To test this, we constructed weighted 'sharing' and 'avoidance' networks of axons. In these networks, each axon is represented as a node, and edge weights were defined by the negative log probabilities of observing the measured degree of target sharing or avoidance under the random model[92], such that stronger weights corresponded to less likely random outcomes.

Upon analyzing these networks, we noted a surprising regularity in their structure. This pattern was present across all developmental stages in our data (P0, $n = 1$; P6–P9, $n = 7$; P60, $n = 1$), except for one notably sparse connectome (P60; see below). It took the form of axons frequently sharing the same targets, forming a linear axonal neighborhood (for example, axon$_1$, axon$_2$, …,axon$_K$; Figs. 1i and 5a,b and Supplementary Figs. 4, 5 and 10). In one adult case (P60), we observed a simpler pattern where many axons repeatedly innervated the same MEFs (Supplementary Fig. 2).

To quantify this regularity and evaluate its statistical significance, we assessed how well the axonal network could be represented on a line such that nearby axons were more likely to share targets and less likely to avoid them. We first computed a two-dimensional spring-force embedding that respected the pairwise innervation patterns. We then quantified its linearity as the variance ratio along the principal axes, calculated as the ratio of the first to second eigenvalues of the covariance matrix of the optimized axonal positions (as in Extended Data Fig. 8).

Comparison of the empirical connectomes with graph distributions using Monte Carlo methods

Unless explicitly stated otherwise, statistical evaluations were performed by comparing developmental connectomes with theoretical graph distributions. This allowed us to estimate the probability of observing our data, or more extreme cases, under null models of random connectivity, particularly when permutation tests within a single connectome were not feasible. Our analysis focused on three principal graph distributions.

The graph distribution used most often in our analysis was the configuration model[93], in which graphs are generated with prescribed nodes and edges corresponding to axons, muscle fibers and their connections. Depending on the biological context, we used either an asymptotic or an exact configuration model. In the asymptotic version, edges were assigned probabilistically according to the node degrees observed in the data. In the exact version, randomly selected stubs were wired algorithmically, and graphs containing self-loops or repeated edges were rejected.

In the asymptotic configuration model, we considered a family of connectomes whose average node degrees matched those in the data. This approach was useful when substantial variability in edge number was biologically plausible across samples. For example, in the newborn connectome, some muscle fibers were innervated by as few as 3 axons and others by as many as 15, while some axons innervated 13 muscle fibers and others up to 120. We therefore used this model to generate a range of random connectomes rather than restricting the analysis to graphs that exactly reproduced the observed motor unit sizes and convergence numbers. This was particularly useful for assessing the linear-order property.

In other cases, variability in node degree would generate biologically implausible networks. For example, in adult connectomes, random graphs that occasionally produced muscle fibers with three or four inputs would not match the data, in which no adult muscle fiber received more than two inputs. For these cases, we used the exact configuration model, which generates connectomes with the same motor unit sizes and convergence numbers as observed in the data. These graphs were then used to compute network properties, including linear order, and to derive estimated *P* values with associated confidence intervals.

When a connectome exhibited a distinctive feature, we compared its graph properties with two sets of random connectomes: those lacking the feature and those reproducing it. For example, adult muscle B showed high centrality (Supplementary Fig. 2). Under random graphs with identical node degrees, axons innervating multiendplate fibers appeared unusually large; however, this difference disappeared when the comparison was restricted to random networks with a similar level of centrality. Thus, the large motor unit sizes in this sample could be explained by its centrality rather than by an independent deviation from the null model. In other special cases, we used permutation or parametric tests as described alongside the corresponding results.

Deriving *P* values under the assumption of noisy CSA measurements

To test whether measurement noise in fiber CSA could bias our Monte Carlo estimate of motor unit force, we first fitted an empirical error model to ground truth volumetric reconstructions of all 213 fibers in an interscutularis muscle (~35 µm each; Supplementary Fig. 18a–c), revealing that the single-section CSA deviates by 7–8% on average (mean bias $\mu = 0.92\%$, $\sigma = 8.39\%$, skew = 0.1; Supplementary Fig. 18d). In every Monte Carlo iteration, we produced a pair of connectomes—the empirical wiring diagram and a degree-preserving randomized counterpart—by independently resampling in both wiring diagrams each fiber's CSA from $N(0, \sigma^2)$ around its measured value. Summed CSA (our force surrogate) was recomputed for both perturbed networks across 10,000 bootstrap resamples, and motor units sharing MEFs remained significantly more similar than expected by chance ($P < 0.001$), confirming that our main conclusion is robust to realistic CSA measurement error in both data and controls.

Statistics and reproducibility

Statistical details for individual analyses are provided in the figure legends, source data or the corresponding Methods subsections. Unless otherwise stated, all statistical tests were two-sided. Sample sizes were determined by the number of independent muscles and by the number of muscle fibers, NMJs or motor units analyzed within each fully reconstructed dataset; no statistical method was used to predetermine sample size. No data were excluded except where explicitly stated in the text or Methods, including a small number of newborn muscle fibers damaged during sample preparation. Experiments were not randomized, except that 52 newborn muscle fibers were randomly selected for myonuclear reconstruction. Blinding was not used during data collection or analysis because connectomic reconstruction requires knowledge of structure identity during annotation and proofreading. Representative images and examples were selected from datasets in which the reported phenomenon was repeatedly observed. Monte Carlo, bootstrap and random-graph procedures are described in the corresponding Methods subsections.

Modeling AP collision as the mechanism to maintain multiple NMJs on the same muscle fiber

We consider a model of AP collision with the following assumptions. (1) When an axonal AP arrives at the presynaptic terminal, it reliably triggers an AP in the muscle fiber, with a synaptic delay T_d between the axonal AP arrival and the onset of the muscular AP. (2) The synaptic delay T_d is identically and independently distributed at the two NMJs on the MEF, following a normal distribution $N(\mu, \sigma^2)$, where μ is the mean synaptic delay and σ is its standard deviation. (3) The muscular AP propagates with a constant speed v_m irrespective of the direction of propagation. We first consider the case in which the two NMJs are innervated by two branches of the same axon. Let the distance from the branching point to the NMJs be l_1 and l_2, respectively. Let the distance between the two NMJs be l_m, so the time for the muscular AP to propagate from one NMJ to the other is given by $T_m = \frac{l_m}{v_m}$. We define the moment when the axonal AP passes the branching point as time $t = 0$. AP collision occurs if, before the muscular AP elicited at NMJ 1 reaches NMJ 2, another muscular AP has been elicited at NMJ 2 but has not arrived at NMJ 1, and vice versa. The time at which the axonal AP elicits a muscular AP at NMJ 1 is $T_1 = \frac{l_1}{v_a} + T_{d1}$, where v_a denotes axonal conduction velocity. Similarly, the time at which the same axonal AP elicits a muscular AP at NMJ 2 is $T_2 = \frac{l_2}{v_a} + T_{d2}$. AP collision occurs only if the absolute difference in onset time between the two muscle fiber APs is smaller than the time it takes a muscle AP to propagate from one NMJ to the other:

$$\Delta T_d = |T_1 - T_2| = \left| \frac{l_1 - l_2}{v_a} + T_{d1} - T_{d2} \right| < \frac{l_m}{v_m}$$

We define $T_a := \frac{l_1 - l_2}{v_a}$ as the difference in axonal arrival time due to unequal path length. Because T_{d1} and T_{d2} are identically and independently distributed normal random variables, their difference, $\Delta T_d := T_{d1} - T_{d2}$, is also normally distributed with mean $\mu_d = 0$ and $\sigma_d = \sqrt{{\sigma_1}^2 + {\sigma_2}^2} = \sqrt{2}\sigma$. This gives the probability of collision:

$$\begin{aligned} P[\text{collision}] &= P[-T_a - T_m < \Delta T_d < -T_a + T_m] \\ &= \frac{1}{2}\left(\operatorname{erf}\frac{-T_a + T_m}{2\sigma} - \operatorname{erf}\frac{-T_a - T_m}{2\sigma}\right), \end{aligned}$$

where erf is the error function. This equation also holds for the case in which two different axons innervate the same MEF at two junctions. In this case, T_a refers to the relative latency between the APs in the two axons.

The expected value of the absolute difference $|T_{d1} - T_{d2}|$ is $\sqrt{\frac{4}{\pi}}\sigma$, which represents the expected time gap of postsynaptic initiation times for two junctions innervated by the same axon, assuming identical arrival times of presynaptic APs at the two nerve terminals.

Reporting summary

Further information on research design is available in the Nature Portfolio Reporting Summary linked to this article.

Data availability

Data supporting the main figures, including interactive 3D reconstructions and image volumes, are available at: https://lichtman.rc.fas.harvard.edu/NMJ_Meirovitch_et_al/. Source data are provided with this paper.

References

68. Feng, G. et al. Imaging neuronal subsets in transgenic mice expressing multiple spectral variants of GFP. *Neuron* **28**, 41–51 (2000).
69. Tapia, J. C. et al. High-contrast en bloc staining of neuronal tissue for field emission scanning electron microscopy. *Nat. Protoc.* **7**, 193–206 (2012).
70. Kasthuri, N. et al. Saturated reconstruction of a volume of neocortex. *Cell* **162**, 648–661 (2015).
71. Hayworth, K. J. et al. Imaging ATUM ultrathin section libraries with WaferMapper: a multi-scale approach to EM reconstruction of neural circuits. *Front. Neural Circuits* **8**, 68 (2014).
72. Eberle, A. L. et al. High-resolution, high-throughput imaging with a multibeam scanning electron microscope. *J. Microsc.* **259**, 114–120 (2015).

73. Saalfeld, S., Fetter, R., Cardona, A. & Tomancak, P. Elastic volume reconstruction from series of ultra-thin microscopy sections. *Nat. Methods* **9**, 717–720 (2012).
74. Rublee, E., Rabaud, V., Konolige, K. & Bradski, G. ORB: an efficient alternative to SIFT or SURF. In *Proc. 2011 International Conference on Computer Vision* 2564–2571 (IEEE, 2011).
75. Fischler, M. A. & Bolles, R. C. Random sample consensus: a paradigm for model fitting with applications to image analysis and automated cartography. *Commun. ACM* **24**, 381–395 (1981) .
76. Lowe, D. G. Object recognition from local scale-invariant features. In *Proc. Seventh IEEE International Conference on Computer Vision*, Vol. 2, 1150–1157 (IEEE, 1999).
77. Berger, D. R., Seung, H. S. & Lichtman, J. W. VAST (Volume Annotation and Segmentation Tool): efficient manual and semi-automatic labeling of large 3D image stacks. *Front. Neural Circuits* **12**, 88 (2018).
78. Duxson, M. J., Usson, Y. & Harris, A. J. The origin of secondary myotubes in mammalian skeletal muscles: ultrastructural studies. *Development* **107**, 743–750 (1989).
79. Pavarino, E. C. et al. mEMbrain: an interactive deep learning MATLAB tool for connectomic segmentation on commodity desktops. *Front. Neural Circuits* **17**, 952921 (2023).
80. Qaisar, R. & Larsson, L. What determines myonuclear domain size? *Indian J. Physiol. Pharmacol.* **58**, 1–12 (2014).
81. Van der Meer, S. F. T., Jaspers, R. T. & Degens, H. Is the myonuclear domain size fixed? *J. Musculoskelet. Neuronal Interact.* **11**, 286–297 (2011).
82. Grady, R. M., Starr, D. A., Ackerman, G. L., Sanes, J. R. & Han, M. Syne proteins anchor muscle nuclei at the neuromuscular junction. *Proc. Natl Acad. Sci. USA* **102**, 4359–4364 (2005).
83. Kay, J. N. et al. Transient requirement for ganglion cells during assembly of retinal synaptic layers. *Development* **131**, 1331–1342 (2004).
84. Arber, S. et al. Requirement for the homeobox gene Hb9 in the consolidation of motor neuron identity. *Neuron* **23**, 659–674 (1999).
85. Schindelin, J. et al. Fiji: an open-source platform for biological-image analysis. *Nat. Methods* **9**, 676–682 (2012).
86. Preibisch, S., Saalfeld, S. & Tomancak, P. Globally optimal stitching of tiled 3D microscopic image acquisitions. *Bioinformatics* **25**, 1463–1465 (2009).
87. Bodine, S. C., Garfinkel, A., Roy, R. R. & Edgerton, V. R. Spatial distribution of motor unit fibers in the cat soleus and tibialis anterior muscles: local interactions. *J. Neurosci.* **8**, 2142–2152 (1988).
88. Roy, R. R. et al. Three-dimensional structure of cat tibialis anterior motor units. *Muscle Nerve* **18**, 1187–1195 (1995).
89. Sharafi, B., Ames, E. G., Holmes, J. W. & Blemker, S. S. Strains at the myotendinous junction predicted by a micromechanical model. *J. Biomech.* **44**, 2795–2801 (2011).
90. Lichtman, J. W. & Wilkinson, R. S. Properties of motor units in the transversus abdominis muscle of the garter snake. *J. Physiol.* **393**, 355–374 (1987).
91. Willshaw, D. J. The establishment and the subsequent elimination of polyneuronal innervation of developing muscle: theoretical considerations. *Proc. R. Soc. Lond. B* **212**, 233–252 (1981).
92. Wang, M., Zhao, Y. & Zhang, B. Efficient test and visualization of multi-set intersections. *Sci. Rep.* **5**, 16923 (2015).
93. Britton, T., Deijfen, M. & Martin-Löf, A. Generating simple random graphs with prescribed degree distribution. *J. Stat. Phys.* **124**, 1377–1397 (2006).

Acknowledgements

We thank the Computational Connectomics Group (CCG) of N. Shavit at MIT CSAIL for discussions on input synchronization. We also thank J. Tian for extensive efforts in reconstructing muscle fibers in the newborn sample; V. Norton for discussions and substantial work on the reconstruction of several axonal arbors; E. Yang for multifaceted contributions to reconstruction of the newborn sample; S. Laskaris for discussions, animal care and preparation of machine learning datasets for muscle fiber expansion and mitochondria classification; T. Tran for axon reconstruction in the EM dataset; J. Brady for assistance with manual axon reconstruction in the EM dataset and for inspiring early discussions on MEFs; M. Badwal for many discussions and early contributions to the research, including reconstruction of the extramuscular dataset; B. Drescher for help in preparing the myonuclei dataset for machine learning; S. Zhou for help with the initial confocal EM analysis and Schwann cell reconstruction in the nerve; and X. Chen for reconstruction of part of the extramuscular bundle and assistance with Schwann cell reconstruction.

Author contributions

Y.M. and J.W.L. conceived the project and hypothesis. Y.M., R.W.D. and K.K. designed the experiments. Y.M., R.W.D., K.K., J.-C.T., S.G.T. and J. Livet generated or provided key reagents and resources. K.K. performed newborn serial-section electron microscopy sample preparation, sectioning and image acquisition, with assistance from R.L.S. A.P. developed the alignment software and aligned the electron microscopy dataset, and Y.W. realigned the dataset for enhanced visualization. R.W.D. performed Brainbow sample preparation, histology and confocal imaging. J.-C.T. and S.G.T. performed developmental and adult YFP/confocal imaging and muscle surveys. Y.M., M.F.H.E., E.C.P. and F.Y. performed newborn axon tracing and motor unit reconstructions. Y.M. performed newborn muscle fiber reconstruction and neuromuscular junction identification. M.M.-C. annotated postsynaptic regions from all neuromuscular junctions in the electron microscopy dataset. Y.M. and M.F.H.E. classified newborn MEFs and SEFs. M.F.H.E. reconstructed newborn myonuclei. Y.M. and K.K. performed newborn Schwann-cell-related reconstructions. F.Y. and Y.M. performed adult axon tracing, motor unit and muscle fiber reconstructions, neuromuscular junction identification, multiple-endplate versus single-endplate muscle fiber classification and myonuclear- and Schwann-cell-related reconstructions. Y.M. performed the connectivity statistics, random-graph and Monte Carlo analyses, cross-sectional area–force analyses, rank order analyses, simulations and figure quantification. D.R.B. contributed to discussions and visualization. Y.M. and J. Lu developed the AP collision model. Y.M. and J.W.L. interpreted the data and wrote the manuscript. J. Lu edited the manuscript. J.W.L. supervised the study and acquired funding.

Funding

This work was supported by NIH grant nos. U01 NS132158, R01 NS133654, R01 NS082525, R01 NS020364, U24 NS109102, UM1 NS132250, RM1 NS132981, U19 NS104653 and R01 NS134846 (J.W.L.); by FONDECYT grant no. 1200951 (J.-C.T.); and by a Spanish Government Temporary Research Stay award (grant no. FPU14/02245; M.M.-C.). The funders had no role in study design, data collection and analysis, decision to publish or preparation of the manuscript.

Competing interests

The authors declare no competing interests.

Additional information

Extended data is available for this paper at https://doi.org/10.1038/s41593-026-02344-7.

Supplementary information The online version contains supplementary material available at https://doi.org/10.1038/s41593-026-02344-7.

Correspondence and requests for materials should be addressed to Yaron Meirovitch or Jeff W. Lichtman.

Peer review information *Nature Neuroscience* thanks Liqun Luo and the other, anonymous, reviewer(s) for their contribution to the peer review of this work.

Reprints and permissions information is available at www.nature.com/reprints.

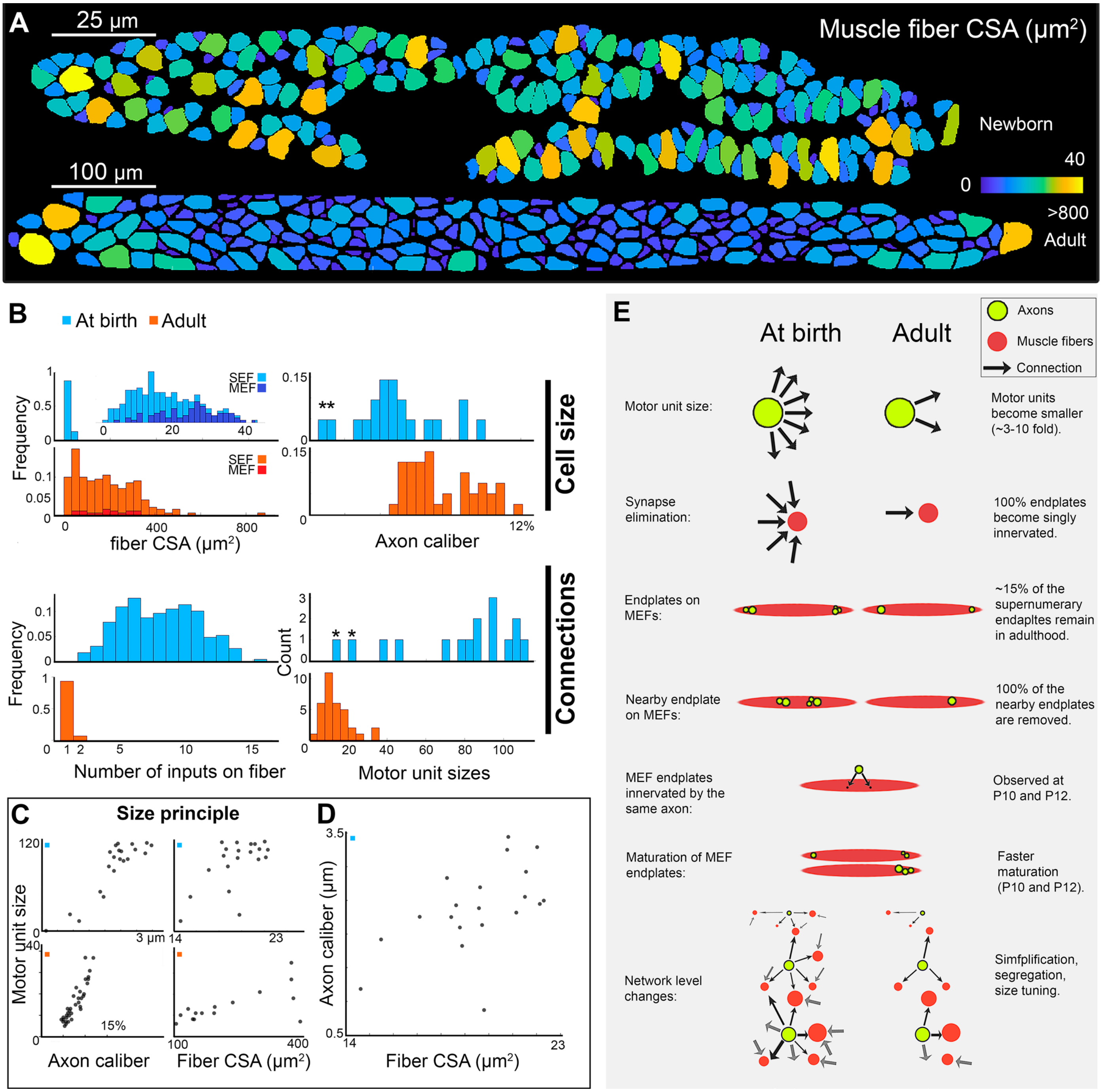

Extended Data Fig. 1 | A size correlation between axons and their innervation targets from birth to adulthood. (**A**) Transverse sections of a newborn and an adult interscutularis muscle. Individual muscle fibers colored by cross-sectional area (CSA). The scale bar indicates the CSA distribution. (**B**) Newborn muscle fibers are ~10% the size of adult muscle fibers. At birth multiple-endplate muscle fibers (MEF) are larger than single-endplate muscle fibers (SEF); this size difference disappears in adulthood. The caliber of motor axons in the newborn shows a bigger distribution in sizes than that of adult axons. The number of distinct axonal inputs onto individual muscle fibers is highly variable (2-15) at birth and reduces to one or two inputs in the adult for SEFs and MEFs, respectively. The motor unit size drastically decreases from birth to adulthood and the shape of the distribution nearly flips. The two smallest neonatal motor units (marked by asterisks) are too small to mature into the large motor units in the adult. (**C to D**) Axon calibers, motor unit sizes, and the average size of innervated muscle fibers are all correlated both at birth and in adulthood, suggesting that features of Henneman's size principle[10] start to emerge in perinatal life. (**E**) Summary of the morphological changes observed in neuromuscular connectomes during postnatal development.

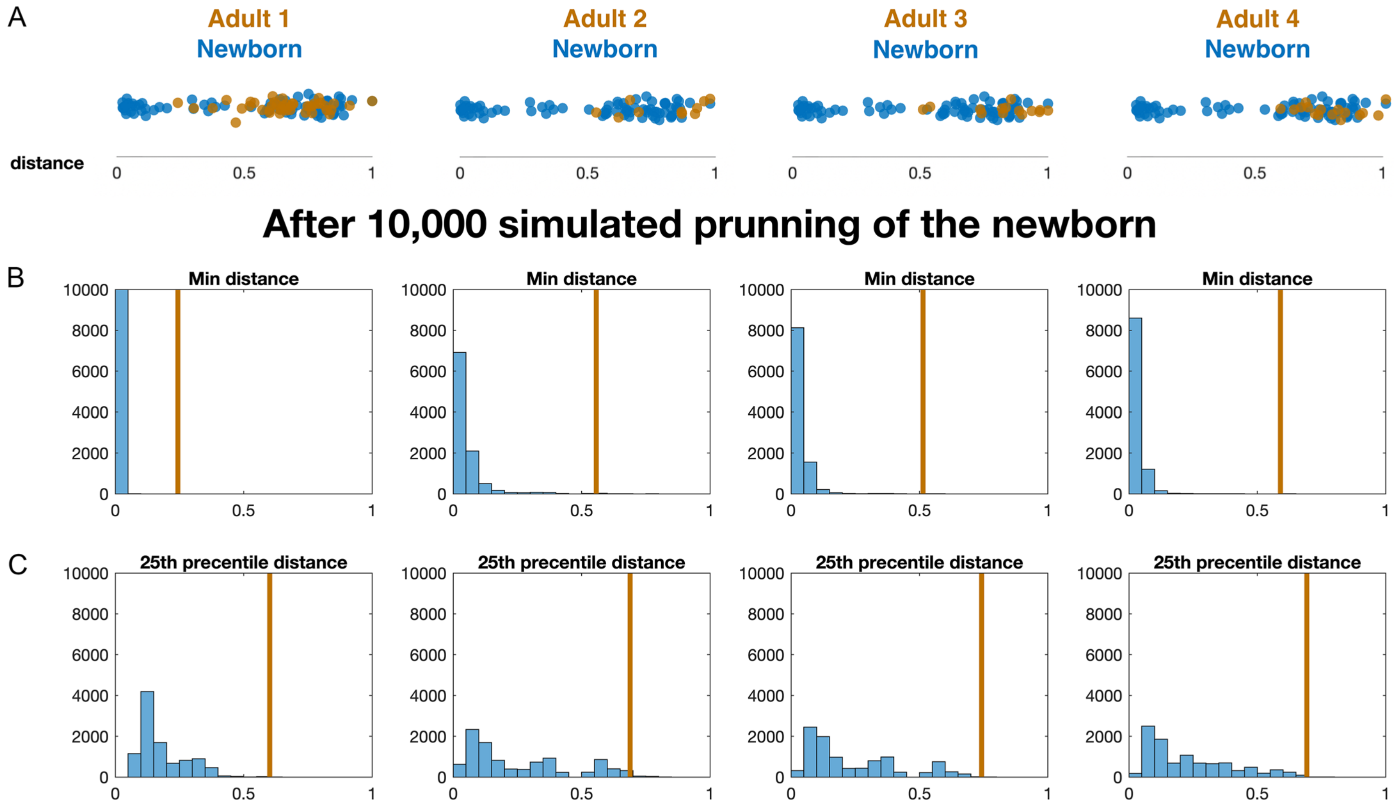

Extended Data Fig. 2 | Adult MEFs preferentially retain NMJs that are farther apart than expected from random attrition. (**A**) Inter-NMJ distances on newborn MEFs (blue) and four adult muscles (brown; Adults 1-4), expressed as a fraction of the maximal newborn distance (1.0). (**B-C**) Distributions of the minimum (B) and first-quartile (C) distances obtained from 10,000 size-matched, without-replacement subsets of the newborn data (blue histograms; bin width = 0.05). The brown line marks the observed statistic in the corresponding adult muscle. In every adult, the statistic lies beyond the 99th percentile of the bootstrap distribution (two-sided Wilcoxon signed-rank, $p < 0.01$), showing a bias toward larger interjunctional separations among the MEFs that persist. Because many widely spaced pairs are nevertheless lost (see Fig. 2) and activity-dependent mechanisms contribute (Fig. 3), distance alone is necessary but not sufficient for NMJ maintenance.

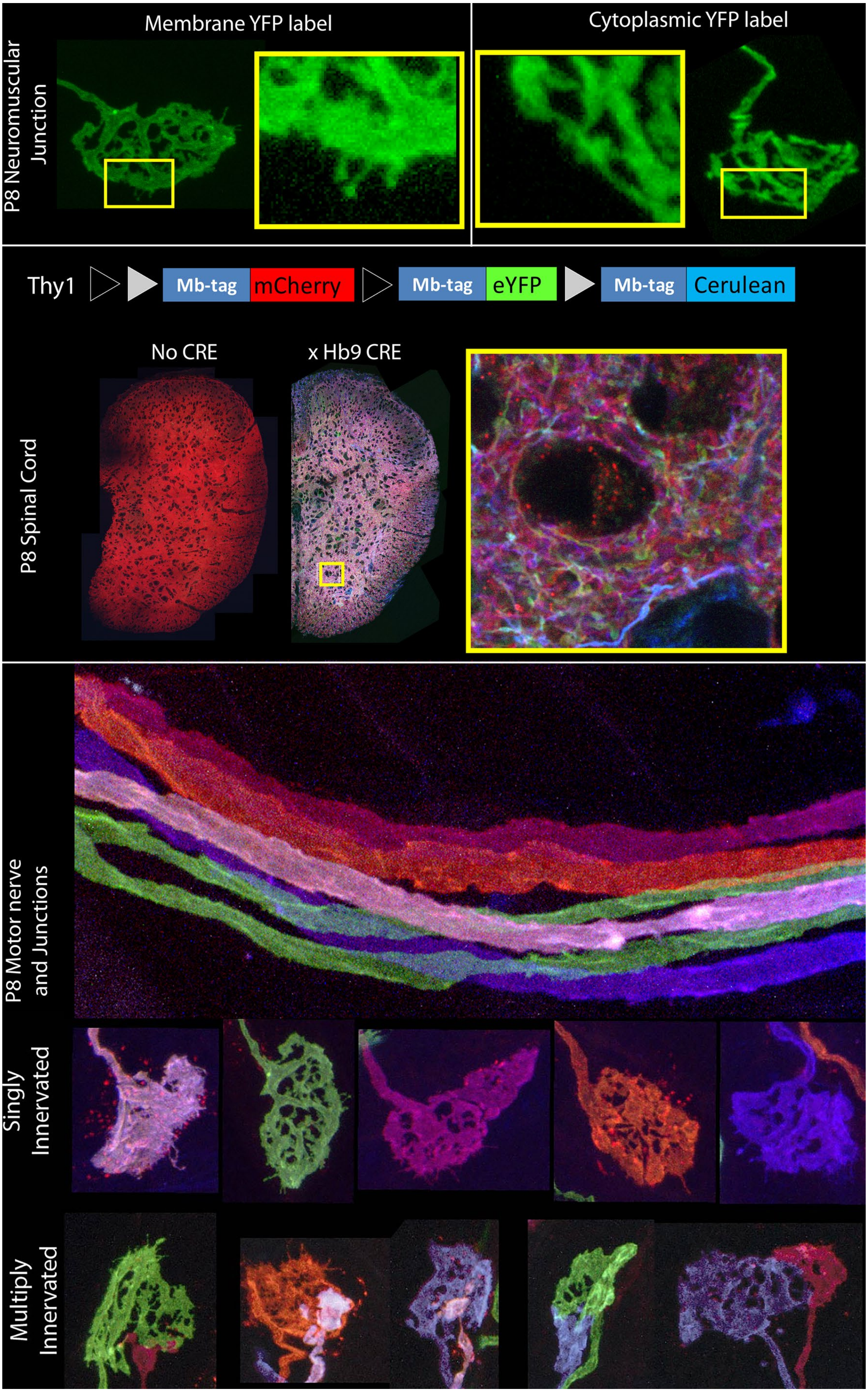

Extended Data Fig. 3 | See next page for caption.

Extended Data Fig. 3 | Membrane-Brainbow expression in developing motor neurons. The top panel shows a schematic of the Brainbow 1.0 type construct. Black and gray triangles indicate Lox P and 2272 sites, respectively. Blue boxes indicate the palmitoylation membrane tag (Mb-tag). The middle panel shows expression of the construct in the spinal cord with and without Cre co-expression. Yellow box shows a high-resolution image of spinal cord neuropil. The bottom panel shows all the motor axons innervating a P9 Omohyoid muscle. Five unique colors and six axon collaterals are easily identifiable (see Methods - Brainbow Histology for details). Below are neuromuscular junctions (NMJs) from the same muscle, both singly and multiply innervated.

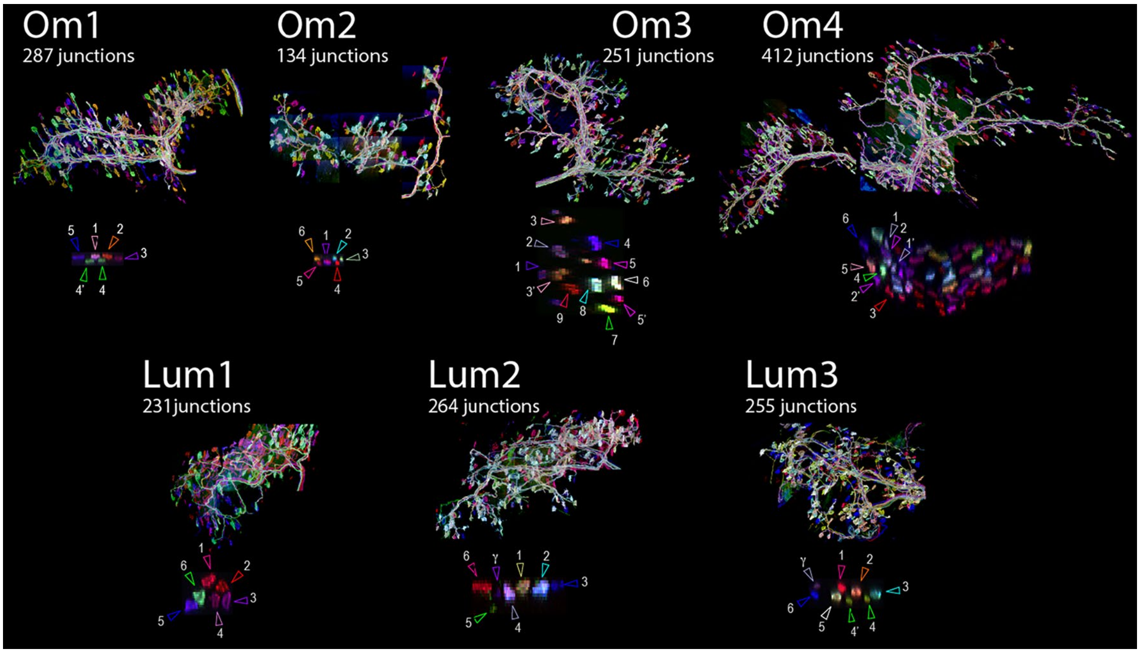

Extended Data Fig. 4 | High resolution confocal image montages of Brainbow labeled P6-9 Omohyoid (Om) and Lumbrical (Lum) muscles. Each panel shows a downsized maximum intensity projection of a high-resolution, four channel three-dimensional image montage that contains all the motor axons and neuromuscular junctions (NMJs) in a developing muscle. Cross sections of the nerve at the muscle entry point are shown, and arrows identify the axons innervating the muscle (γ indicates a gamma motor axon; an apostrophe indicates a putative axon collateral; see Methods).

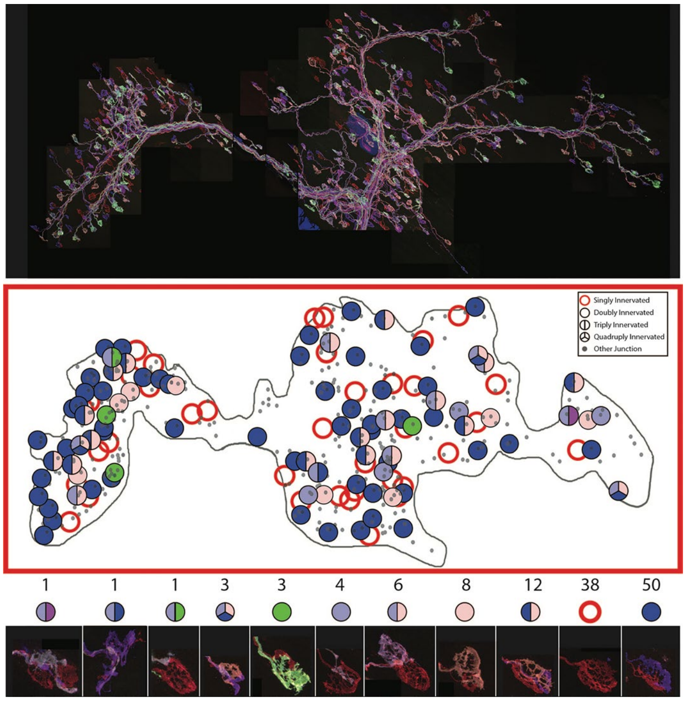

Extended Data Fig. 5 | A map of all terminals of one developing motor axon. Top panel shows the maximum intensity projection of a P6 Omohyoid muscle (Om4). The identity of all axon terminals was determined based on color. The locations of all neuromuscular junctions (NMJs) are shown as small gray dots. The locations of NMJs innervated by the red axon are shown as large colored circles. The color of the circles indicates the identity of other axons innervating the same NMJ. The bottom panel shows images of each category of NMJ as well as the numbers of NMJs in each category.

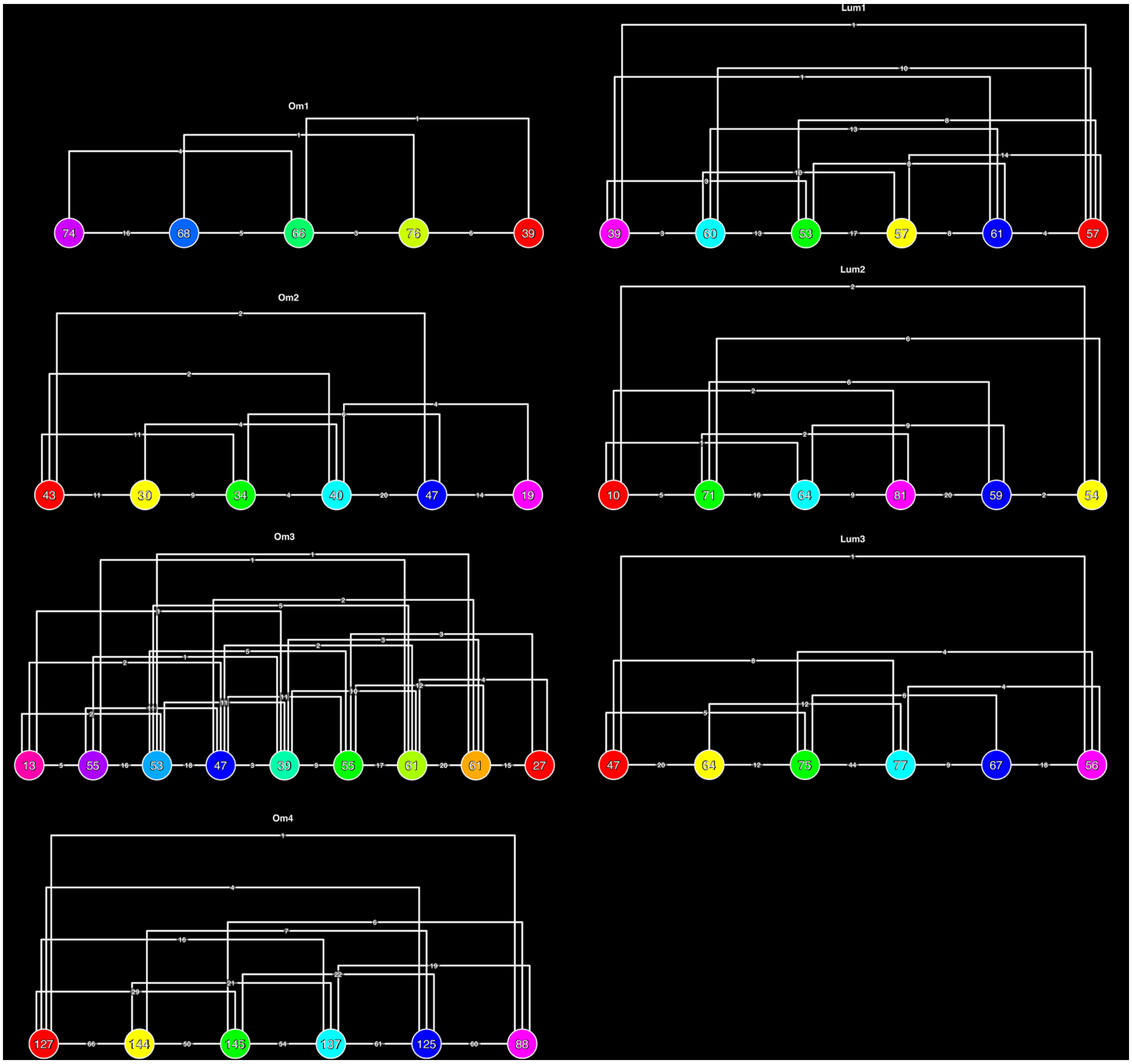

Extended Data Fig. 6 | Connectivity of rank-ordered motor axons in seven developing muscles (P6–P9). Circles denote individual motor axons, each labeled with the number of muscle fibers it innervates; lines between circles indicate, for every axon pair, the number of co-innervated muscle fibers.

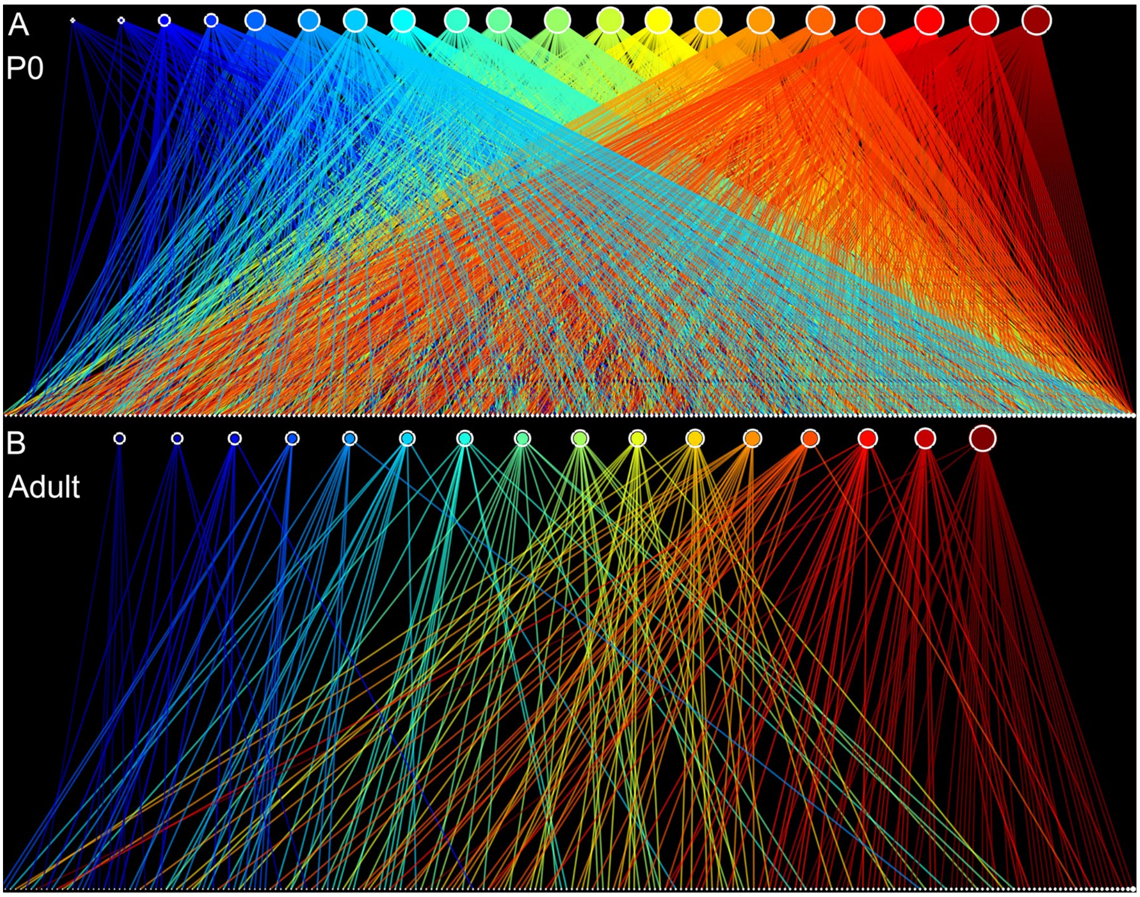

Extended Data Fig. 7 | Global simplification of the neuromuscular connectome from birth to adulthood. (**A**) Dense connectivity between motor neurons (top row) and muscle fibers (bottom row) at birth. Warmer colors indicate larger motor units. (**B**) Profound simplification of the same two-layer graph by 4 weeks of age.

https://doi.org/10.1038/s41593-026-02344-7

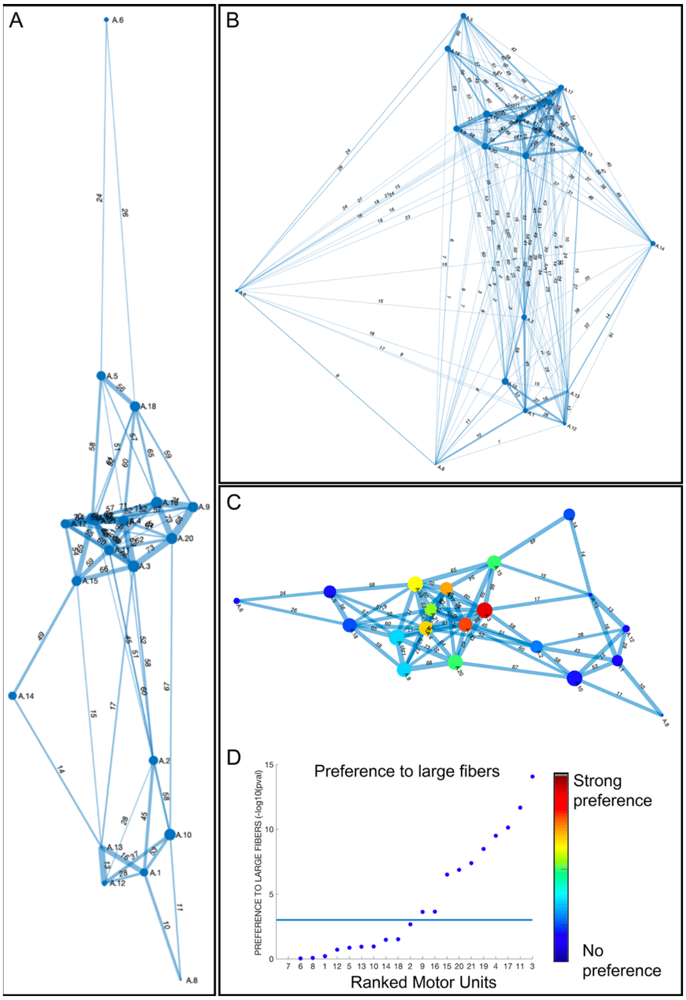

Extended Data Fig. 8 | Linear orders in the newborn dataset using alternative scales. (**A**) Linear orders based on axon pair tendencies to share muscle fibers, considering statistically significant edges under the random connectome model ($p < 0.01$). The resulting diagram is elongated, indicating a linear ordering of axons based on their tendency to share targets with other axons that are placed next to them in the diagram. (**B**) Linear orders including all edges show similar tendencies. (**C** to **D**) Ranking units based on their preference to innervate large fibers reveals that the linear order is organized according to peripheries that show no preference to large muscle fibers and a central cluster with motor units that are highly selective to large muscle fibers. This suggests that the newborn linear order is consistent with the structural properties of the muscle fibers. Moreover, even when a large motor unit, such as motor unit 10, is not selective to muscle fiber size, it is still part of the periphery of the linear order.

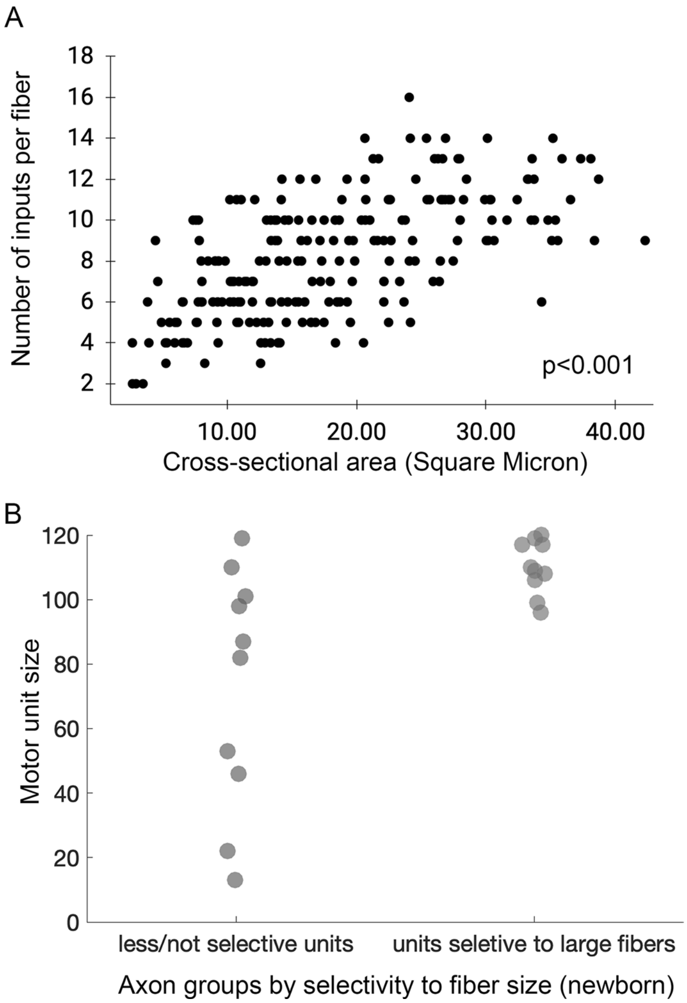

Extended Data Fig. 9 | Association between muscle fiber size, number of inputs and motor unit size in the newborn. (**A**) A correlation between cross-sectional area of muscle fibers and the number of distinct axons innervating them. (**B**) Half of the motor units (*N* = 10) were selectively innervating large muscle fibers ($p < 0.01$); none of the small motor units was selective to large fibers and ~half of the non-selective units were large motor units.

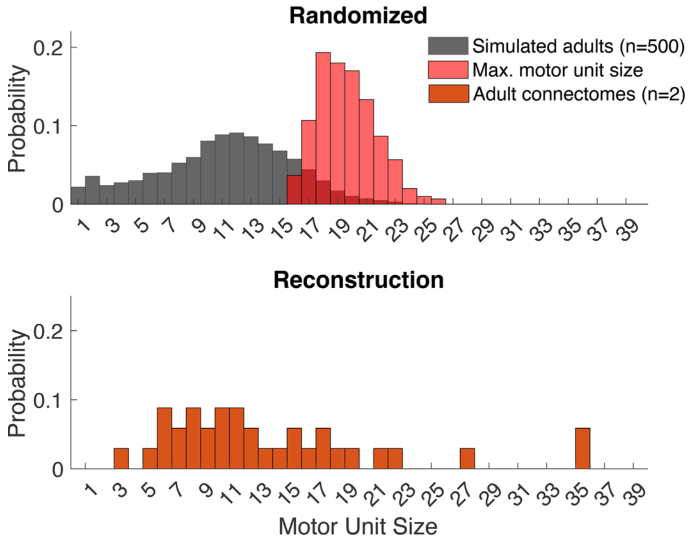

Extended Data Fig. 10 | Simulated synapse elimination in the newborn connectome cannot reproduce adult motor-unit sizes. (top) Histogram of motor unit sizes from 300 simulated adult connectomes (gray) generated by iteratively removing synapses at random from the newborn connectome (Fig. 6c, Extended Data Fig. 7). The overlaid red histogram provides, for each simulation, the size of its largest motor unit. **(bottom)** Motor-unit size distribution in the two adult interscutularis connectomes reconstructed here (as in Extended Data Fig. 1) and consistent with the six adult connectomes in ref. 16. The largest biological motor units (35 and 36 fibers) never arise in the random-elimination simulations (simulation mean 20.09 ± 2.05 fibers; $p < 0.01$, 0/300 occurrences).

nature portfolio

Corresponding author(s): Yaron Meirovitch; Jeff Lichtman

Last updated by author(s): Apr 22, 2026

Reporting Summary

Nature Portfolio wishes to improve the reproducibility of the work that we publish. This form provides structure for consistency and transparency in reporting. For further information on Nature Portfolio policies, see our Editorial Policies and the Editorial Policy Checklist.

Statistics

For all statistical analyses, confirm that the following items are present in the figure legend, table legend, main text, or Methods section.

n/a	Confirmed	
☒	☐	The exact sample size (*n*) for each experimental group/condition, given as a discrete number and unit of measurement
☐	☒	A statement on whether measurements were taken from distinct samples or whether the same sample was measured repeatedly
☐	☒	The statistical test(s) used AND whether they are one- or two-sided *Only common tests should be described solely by name; describe more complex techniques in the Methods section.*
☒	☐	A description of all covariates tested
☒	☐	A description of any assumptions or corrections, such as tests of normality and adjustment for multiple comparisons
☐	☒	A full description of the statistical parameters including central tendency (e.g. means) or other basic estimates (e.g. regression coefficient) AND variation (e.g. standard deviation) or associated estimates of uncertainty (e.g. confidence intervals)
☐	☒	For null hypothesis testing, the test statistic (e.g. *F*, *t*, *r*) with confidence intervals, effect sizes, degrees of freedom and *P* value noted *Give P values as exact values whenever suitable.*
☒	☐	For Bayesian analysis, information on the choice of priors and Markov chain Monte Carlo settings
☒	☐	For hierarchical and complex designs, identification of the appropriate level for tests and full reporting of outcomes
☐	☒	Estimates of effect sizes (e.g. Cohen's *d*, Pearson's *r*), indicating how they were calculated

Our web collection on statistics for biologists contains articles on many of the points above.

Software and code

Policy information about availability of computer code

Data collection: ZEISS ZEN 2010, Olympus FV10-ASW 4.1, Fiji/ImageJ, Imaris

Data analysis: MATLAB, Fiji/ImageJ, Imaris, VAST, mEMbrain

For manuscripts utilizing custom algorithms or software that are central to the research but not yet described in published literature, software must be made available to editors and reviewers. We strongly encourage code deposition in a community repository (e.g. GitHub). See the Nature Portfolio guidelines for submitting code & software for further information.

Data

Policy information about availability of data

All manuscripts must include a data availability statement. This statement should provide the following information, where applicable:

- Accession codes, unique identifiers, or web links for publicly available datasets
- A description of any restrictions on data availability
- For clinical datasets or third party data, please ensure that the statement adheres to our policy

Data supporting the main figures, including interactive 3D reconstructions and image volumes, are available at the Lichtman laboratory website: https://lichtman.rc.fas.harvard.edu/NMJ_Meirovitch_et_al/. Source data underlying quantitative plots are provided with the paper.

Research involving human participants, their data, or biological material

Policy information about studies with human participants or human data. See also policy information about sex, gender (identity/presentation), and sexual orientation and race, ethnicity and racism.

Reporting on sex and gender	This study did not involve human participants, human data, or human biological material.
Reporting on race, ethnicity, or other socially relevant groupings	This study did not involve human participants, human data, or human biological material.
Population characteristics	This study did not involve human participants, human data, or human biological material.
Recruitment	This study did not involve human participants, human data, or human biological material.
Ethics oversight	This study did not involve human participants, human data, or human biological material.

Note that full information on the approval of the study protocol must also be provided in the manuscript.

Field-specific reporting

Please select the one below that is the best fit for your research. If you are not sure, read the appropriate sections before making your selection.

☒ Life sciences ☐ Behavioural & social sciences ☐ Ecological, evolutionary & environmental sciences

For a reference copy of the document with all sections, see nature.com/documents/nr-reporting-summary-flat.pdf

Life sciences study design

All studies must disclose on these points even when the disclosure is negative.

Sample size	Sample sizes were determined by the number of muscles, motor units, muscle fibers, and neuromuscular junctions that could be fully reconstructed for each experiment using the relevant connectomic method. No statistical method was used to predetermine sample size. The newborn connectome was reconstructed from one ssEM dataset, the intermediate developmental Brainbow analysis included 7 muscles, and the developmental/adult confocal analyses included more than 20 muscles across ages. For each reconstructed dataset, all relevant neurons, fibers, and/or junctions within the analyzed volume were included, and n is reported in the manuscript, figure legends, or tables.
Data exclusions	No data were excluded except where explicitly stated in the manuscript or Methods, including a small number of newborn muscle fibers damaged during sample preparation.
Replication	Fully reconstructed datasets from multiple muscles and developmental stages were analyzed. Adult confocal reconstructions were consistent with previous results for the interscutularis muscle. For each dataset, the reported phenomena were observed repeatedly within the reconstructed sample(s), and representative examples were selected from datasets in which the phenomenon was repeatedly observed.
Randomization	Experiments were not randomized, except that 52 newborn muscle fibers were randomly selected for myonuclear reconstruction. Each reconstructed muscle was treated as an independent sample. For some analyses, empirical connectomes were compared with random connectomes generated by Monte Carlo or configuration-model methods, as described in the Methods,
Blinding	Blinding was not used during data collection or analysis because connectomic reconstruction, annotation, and proofreading require knowledge of structure identity. Where reconstructions or annotations were performed, multiple annotators and quality-control procedures were used as described in the Methods.

Reporting for specific materials, systems and methods

We require information from authors about some types of materials, experimental systems and methods used in many studies. Here, indicate whether each material, system or method listed is relevant to your study. If you are not sure if a list item applies to your research, read the appropriate section before selecting a response.

Materials & experimental systems

n/a	Involved in the study	
☐	☒	Antibodies
☒	☐	Eukaryotic cell lines
☒	☐	Palaeontology and archaeology
☐	☒	Animals and other organisms
☒	☐	Clinical data
☒	☐	Dual use research of concern
☒	☐	Plants

Methods

n/a	Involved in the study	
☒	☐	ChIP-seq
☒	☐	Flow cytometry
☒	☐	MRI-based neuroimaging

Antibodies

Antibodies used	Fluorescently tagged anti-myosin I immunoglobulin was used to identify slow muscle fibers in three P8–P9 lumbrical muscles.
Validation	The anti-myosin I immunoglobulin was used for established identification of slow muscle fibers based on its expected labeling pattern in lumbrical muscle.

Animals and other research organisms

Policy information about studies involving animals; ARRIVE guidelines recommended for reporting animal research, and Sex and Gender in Research

Laboratory animals	Mus musculus was used in this study. Thy1-YFP16 transgenic mice (B6.Cg-Tg(Thy1-YFP)16Jrs/J; JAX 003709) were used for developmental and adult confocal imaging. Hb9-Cre mice (JAX 006600) were crossed with Thy1-Membrane-Brainbow animals generated as described in the manuscript for Brainbow experiments. Postnatal ages analyzed included birth/P0, P1, P3, P5, P6–P9, P10, P12, P30, and P60.
Wild animals	This study did not involve wild animals.
Reporting on sex	Sex was not recorded for these experiments.
Field-collected samples	This study did not involve field-collected samples.
Ethics oversight	Animal procedures were conducted according to the guidelines of the Harvard Animal Care and Use Committee (IACUC).

Note that full information on the approval of the study protocol must also be provided in the manuscript.

Plants

Seed stocks	This study did not involve plants.
Novel plant genotypes	This study did not involve plants.
Authentication	This study did not involve plants.